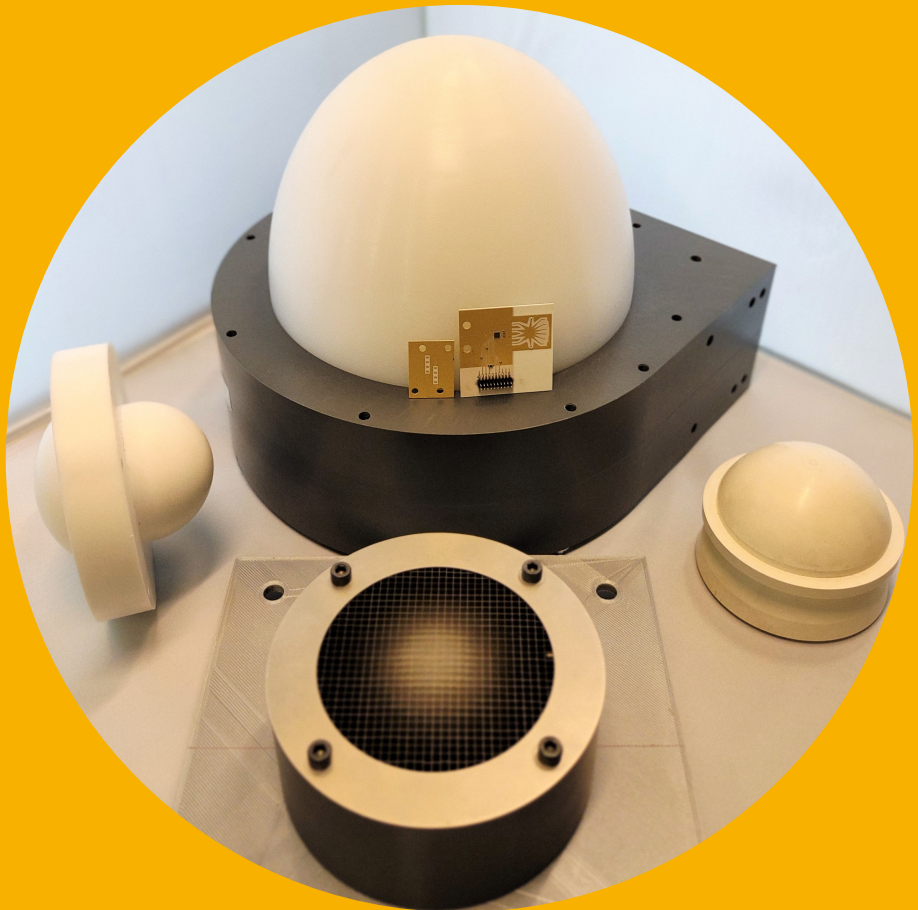


# Beam-switching antennas for millimeter-wave communications

---

Sabin Kumar Karki



# Beam-switching antennas for millimeter-wave communications

**Sabin Kumar Karki**

A doctoral dissertation completed for the degree of Doctor of Science (Technology) to be defended, with the permission of the Aalto University School of Electrical Engineering, at a public examination held via a remote connection on 22 October 2021 at 12.

**Aalto University**  
**School of Electrical Engineering**  
**Department of Electronics and Nanoengineering**

**Supervising professor**

Prof. Ville Viikari, Aalto University, Finland

**Thesis advisor**

Dr. Juha Ala-Laurinaho, Aalto University, Finland

**Preliminary examiners**

Dr. Alexey Artemenko, Radio Gigabit LLC, Russia

Dr. Benjamin Fuchs, University of Rennes 1, France

**Opponent**

Prof. Fabien Ferrero, Université Côte d'Azur, France

Aalto University publication series

**DOCTORAL DISSERTATIONS** 137/2021

© 2021 Sabin Kumar Karki

ISBN 978-952-64-0539-1 (printed)

ISBN 978-952-64-0540-7 (pdf)

ISSN 1799-4934 (printed)

ISSN 1799-4942 (pdf)

<http://urn.fi/URN:ISBN:978-952-64-0540-7>

Images: Sabin Kumar Karki

Unigrafia Oy

Helsinki 2021

Finland



**Author**

Sabin Kumar Karki

**Name of the doctoral dissertation**

Beam-switching antennas for millimeter-wave communications

**Publisher** School of Electrical Engineering**Unit** Department of Electronics and Nanoengineering**Series** Aalto University publication series DOCTORAL DISSERTATIONS 137/2021**Field of research** Radio Engineering**Manuscript submitted** 1 June 2021**Date of the defence** 22 October 2021**Permission for public defence granted (date)** 7 September 2021**Language** English☐ **Monograph**☒ **Article dissertation**☐ **Essay dissertation****Abstract**

Millimeter-wave frequencies, i.e. 30-300 GHz, are being widely adopted in commercial applications such as communication systems, radar, and imaging. At millimeter-wave frequencies, the antennas need to be directive to mitigate the higher free-space loss and atmospheric attenuation. In addition, the beam steering capability helps to extend the coverage to a wide angular range.

The objective of the thesis is to develop high-gain and wide beam-steering antennas based on the beam-switching topology. The thesis contributes to the improvement of the integrated lens antenna (ILA) and the feed beam-switching network (BSN) performance. The ILAs are evaluated in terms of form-factor and scan-loss reduction and efficiency improvement. The study of BSN is aimed towards insertion loss reduction and enabling beam reconfigurability.

An elliptical ILA with a focal length to diameter ratio,  $f/d$ , of 1.1 and a diameter of 160 mm is designed to meet the gain and beam-steering regulations for the point-to-point link antennas operating at 71-76 GHz. The  $f/d$  of an elliptical ILA is reduced to 0.88 by using the high permittivity material. An integrated metal-plate lens (IMLA), a combination of the dielectric and metal-plate lens, is proposed to reduce the focal length. The IMLA with 0.69  $f/d$  is designed to achieve a total efficiency of 64% in comparison to 45% of the traditional ILA. The radiation pattern tilting of the offset feeds along the focal plane improved the scan loss of the IMLA by 3.5 dB compared to a traditional ILA. Furthermore, the reduction of scan loss and the extension of the beam steering range of the hemispherical ILA is achieved by positioning the feeds along the spherical surface.

The second part of the thesis focuses on the BSN. The numerical study demonstrates that the ILA radiation properties are mostly affected by the radiation pattern distortion of the beam-switching feed array rather than the coupling between the feed ports. The BSN of the Rotman lens fed array is implemented with the 4-channel vector modulator (VM) instead of the RF-switch to minimize the insertion loss. The Rotman lens-based array uses the 1×4 SIW-fed microstrip patch antenna arrays as the radiating elements and a novel easy-to-implement admittance control mechanism is demonstrated for the SIW-fed series arrays. The beam-configurability of the Rotman lens-based array is attained by simultaneous excitation of the beam ports with the VM, which varies the half power beamwidth from 18° to 75°.

**Keywords** beam reconfigurable, beam-switching, integrated lens antenna, low-profile, millimeter-wave antennas, Rotman lens, scan loss

**ISBN (printed)** 978-952-64-0539-1**ISBN (pdf)** 978-952-64-0540-7**ISSN (printed)** 1799-4934**ISSN (pdf)** 1799-4942**Location of publisher** Helsinki**Location of printing** Helsinki **Year** 2021**Pages** 160**urn** <http://urn.fi/URN:ISBN:978-952-64-0540-7>





# Preface

The research presented in this doctoral thesis has been conducted in the Department of Electronics and Nanoengineering, Aalto University School of Electrical Engineering in 2017-2021. The research activities were funded by the Nokia Bell Labs, Business Finland, and Academy of Finland through the ELens, 5WAVE, and ADENN projects. Furthermore, I am grateful to have received personal grants from the Nokia Foundation and Walter Ahlström Foundation.

I am grateful to Professor Ville Viikari for providing me the opportunity to join the research group as a Master's Thesis student which continued to this doctoral study. I would like to extend my deepest gratitude towards my advisor Dr. Juha Ala-Laurinaho who believed in me, continuously encouraged, and guided me during the doctoral research. I would also like to thank co-authors of the publications Dr. Aki Karttunen, Dr. Antti Lamminen, Dr. Markku Lahti, Dr. Risto Valkonen, Mr. Mikko Kaunisto, Dr. Jianfang Zheng, Dr. Jussi Säily, Dr. Mikko Varonen, Dr. Mikko Kantanen, Mr. Arto Rantala, and Mr. Manu Lahdes for their effort and cooperation. I am also thankful to Mr. Eino Kahra and Mr. Matti Vaaja for their help in the design of the mechanical structures and measurements.

I would also like to offer my special thank you to my colleagues Mr. Jaakko Haarla, Dr. Jari-Matti Hannula, Mr. Henri Kähkönen, Mr. Riku Kormilainen, Dr. Joni Kurvinen, Mr. Veli-Pekka Kutinlahti, Dr. Mikko Leino, Dr. Rasmus Luomaniemi, and Dr. Resti Montoya Moreno for the fruitful discussions and creating the enjoyable working environment. A big thanks to Dr. Jari Holopainen for taking me as an assistant in the Antennas Workshop course and sharing his enthusiasm for teaching. I appreciate efforts of the preliminary examiners Dr. Benjamin Fuchs and Dr. Alexey Artemenko for providing valuable comments to improve the thesis. I would also like to express sincere gratitude to Prof. Fabien Ferrero for agreeing to act as the opponent to this thesis.

Thank you very much Dr. Pramodh Bhusal for all the guidances inside and outside of work. I would like to thank the group of friends Subin Bhandari, Shishir Bhattarai, Pravesh Chand, Dixit KC, Irfan Khan, Janaki Prasad Koirala, Binda Pandey, Merlin Samy, Ganesh Sharma, and Tekendra Timsina for all the support and social events that has made this journey enjoyable. Special thanks

to Rajesh Poudel for the camaraderie and conversations about life in general. To my friends scattered around the world Binayak, Nishiv, Pawan, Peeyush, and Ronam, it is fun and entertaining to have friends like you.

I would like to acknowledge the constant support that I receive from my family. Daddy Krishna Bahadur Karki, mommy Bimala Karki, and brother Saroj Karki I am fortunate to have a family like you. Finally, to my wife Smarika KC, who has been by my side since the beginning of this doctoral study and has seen all the ups and downs. I would like to express gratitude for the support and encouragement I receive, this success also belongs to you.

Espoo, September 26, 2021,

Sabin Kumar Karki

# Contents

<b>Preface</b>	<b>1</b>
<b>Contents</b>	<b>3</b>
<b>List of Publications</b>	<b>5</b>
<b>Author's Contribution</b>	<b>7</b>
<b>List of Abbreviations and Symbols</b>	<b>11</b>
<b>1. Introduction</b>	<b>15</b>
1.1 Introduction . . . . .	15
1.2 Objective and impact . . . . .	16
1.3 Scientific merits . . . . .	17
1.4 Structure of dissertation . . . . .	17
<b>2. High gain antennas</b>	<b>19</b>
2.1 Antenna parameter . . . . .	19
2.2 High-gain and beam-steering antennas . . . . .	21
2.2.1 Phased array antenna . . . . .	21
2.2.2 Beam-switching antennas . . . . .	23
2.3 Integrated lens antenna . . . . .	24
2.3.1 Design . . . . .	25
2.3.2 Scan loss . . . . .	27
2.3.3 Area of focal plane array . . . . .	29
2.4 Antenna design . . . . .	30
2.4.1 Design and simulation . . . . .	30
2.4.2 Measurement . . . . .	31
<b>3. Low-profile and low scan loss integrated lens antenna</b>	<b>33</b>
3.1 Introduction . . . . .	33
3.2 Integrated lens antenna for backhaul application . . . . .	34
3.3 Effect of material properties . . . . .	37
3.4 Dual-spherical integrated lens antenna . . . . .	39

3.5	Integrated metal-plate lens . . . . .	41
3.5.1	Volumetric analysis . . . . .	41
3.5.2	Fabrication . . . . .	44
3.5.3	Scan-loss reduction . . . . .	47
<b>4.</b>	<b>Beam-switching network</b>	<b>51</b>
4.1	Introduction . . . . .	51
4.2	Effect of feed mutual coupling on ILA . . . . .	52
4.3	Beam-reconfigurable antenna with Rotman lens . . . . .	56
4.3.1	SIW-fed $1 \times 4$ series array . . . . .	57
4.3.2	Vertical transition . . . . .	59
4.3.3	Vector modulator IC as RF switch . . . . .	59
4.3.4	Beam-reconfigurability . . . . .	61
<b>5.</b>	<b>Summary of publications</b>	<b>65</b>
<b>6.</b>	<b>Conclusions</b>	<b>69</b>
	<b>References</b>	<b>71</b>
	<b>Errata</b>	<b>79</b>
	<b>Publications</b>	<b>81</b>

# List of Publications

This thesis consists of an overview and of the following publications which are referred to in the text by their Roman numerals.

- I** S. K. Karki, J. Ala-Laurinaho, V. Viikari, and R. Valkonen, "Lens Antenna Design for E-band Point-to-point Radio Links," in *Proceedings of the 38th Progress In Electromagnetics Research Symposium - Spring (PIERS)*, St. Petersburg, Russia, 22-25 May 2017, pp. 1625-1631.
- II** S. K. Karki, J. Ala-Laurinaho, A. Karttunen, and V. Viikari, "Integrated Lens Antennas for E-band," in *Proceedings of the 48th European Microwave Conference (EuMC)*, Madrid, Spain, 23-27 Sept. 2018, pp. 1151-1154.
- III** A. E. I. Lamminen, S. K. Karki, A. Karttunen, M. Kaunisto, J. Säily, M. Lahdes, J. Ala-Laurinaho, and V. Viikari, "Beam-Switching Dual-Spherical Lens Antenna with Low Scan Loss at 71–76 GHz," *IEEE Antennas and Wireless Propagation Letters*, vol. 17, no. 10, pp. 1871-1875, October 2018.
- IV** S. K. Karki, J. Ala-Laurinaho, and V. Viikari, "Integrated Metal-lens Antennas with Reduced Height at 71–76 GHz," in *Proceedings of the 13th European Conference on Antennas and Propagation (EuCAP)*, Krakow, Poland, 31 Mar.-5 Apr. 2019, pp. 1-5.
- V** S. K. Karki, J. Ala-Laurinaho, and V. Viikari, "Low-profile Scanloss-Reduced Integrated Metal-Lens Antenna," *IEEE Transactions on Antennas and Propagation*, 2021, 12 pages.
- VI** S. K. Karki, J. Ala-Laurinaho, V. Viikari, and R. Valkonen, "Effect of Mutual Coupling Between Feed Elements on Integrated Lens Antenna Performance," *IET Microwaves, Antennas & Propagation*, vol. 12, no. 10, pp. 1649-1655, August 2018.
- VII** S. K. Karki, M. Varonen, M. Kaunisto, A. Rantala, M. Lahti, A. Lamminen, J. Holmberg, M. Kantanen, J. Ala-Laurinaho, and V. Viikari, "Beam-Reconfigurable Antenna Based on Vector Modulator and Rotman Lens on LTCC," *IEEE Access*, vol. 9, pp. 52872-52882, March 2021.

- VIII** S. K. Karki, J. Ala-Laurinaho, J. Zheng, M. Lahti, and V. Viikari, “Millimeter-Wave Stepped Series Array with LTCC,” in *Proceedings of the 49th European Microwave Conference (EuMC)*, Paris, France, 1-3 Oct. 2019, pp. 956-959.

# Author's Contribution

## **Publication I: “Lens Antenna Design for E-band Point-to-point Radio Links”**

This work and publication is a collaborative effort. The author performed the simulations and designed the integrated lens antenna. The measurements were jointly done by the author and Dr. Ala-Laurinaho. The author had a major responsibility in preparing the manuscript. Dr. Ala-Laurinaho also instructed the work, and Prof. Viikari supervised the work.

## **Publication II: “Integrated Lens Antennas for E-band”**

The author performed the simulation studies and designed the integrated lens antenna with the PREPERM L450 material. The ILA with Rexolite material was designed by Dr. Karttunen. The author conducted the measurements and had a major role in preparing the paper. Dr. Ala-Laurinaho instructed the work, and Prof. Viikari supervised the work.

## **Publication III: “Beam-Switching Dual-Spherical Lens Antenna with Low Scan Loss at 71–76 GHz”**

This publication is the result of collaborative work. Dr. Karttunen designed the dual-spherical lens. The full-wave simulation of dual-spherical ILA,  $1 \times 16$  beam-switching array design and its characterization were performed by VTT team. The author conducted the measurements of the lens antenna, analysed the results, and had a major responsibility in preparing the manuscript. Dr. Ala-Laurinaho instructed the work, and Prof. Viikari supervised the work.



#### **Publication IV: “Integrated Metal-lens Antennas with Reduced Height at 71–76 GHz”**

The author proposed the idea, performed the simulation studies, and designed the integrated metal-plate lens antenna (IMLA). The author had a major responsibility to prepare the manuscript. Dr. Ala-Laurinaho instructed the work, and Prof. Viikari supervised the work.

#### **Publication V: “Low-profile Scanloss-Reduced Integrated Metal-Lens Antenna”**

The author was responsible for designing the IMLA, assembling the metal-plate lens, and measuring the IMLA. He also designed the square-waveguide feed and the technique to tilt the feed radiation pattern. The author had a major responsibility to prepare the manuscript. Dr. Ala-Laurinaho helped to analyse the measurement results and instructed the work. Prof. Viikari supervised the work.

#### **Publication VI: “Effect of Mutual Coupling Between Feed Elements on Integrated Lens Antenna Performance”**

The idea originated from a joint discussion with Dr. Ala-Laurinaho and Dr. Risto Valkonen. The author designed and simulated the feed antenna array, performed the ray-tracing simulations, and wrote the paper. Dr. Ala-Laurinaho instructed the work and participated in analysing the results. Prof. Viikari supervised the work.

#### **Publication VII: “Beam-Reconfigurable Antenna Based on Vector Modulator and Rotman Lens on LTCC”**

The work and publication are a collaborative effort. The idea originally came from a joint discussion with Dr. Ala-Laurinaho and Dr. Lamminen. The author designed and simulated the Rotman lens-based beam-switching antenna array. The design of the 4-channel vector modulator, design of control and biasing circuit, fabrication of LTCC module, and VM assembly were done by the VTT team. The author had major responsibility for preparing the manuscript and Dr. Varonen assisted in writing the part concerning the vector modulator design. Dr. Ala-Laurinaho advised the work and supported in analysing the results. Prof. Viikari supervised the work.

**Publication VIII: “Millimeter-Wave Stepped Series Array with LTCC”**

This publication is a joint effort. The author designed and simulated the series arrays. Dr. Lahti was responsible for the antenna fabrication. The near-field measurements were done by the author, whereas the probe station gain measurement was done by Dr. Zheng. The author had the main responsibility of preparing the manuscript. Dr. Ala-Laurinaho instructed the work, and Prof. Viikari supervised the work.



# List of Abbreviations and Symbols

## Abbreviations

1D	One-dimensional
2D	Two-dimensional
3D	Three-dimensional
3GPP	3rd Generation Partnership Project
5G	5th Generation
ACMPA	Aperture Coupled Microstrip Patch Antenna
AUT	Antenna Under Test
BFN	Beam-Forming Network
BSA	Beam-Switching Antenna
BSN	Beam-Switching Network
CNC	Computer Numerical Control milling machine
EA	Embedded Aperture coupled microstrip patch antenna
E-band	Frequency band 60-90 GHz
EM	Electromagnetic
ESA	Embedded Stacked Aperture coupled microstrip patch antenna
FPA	Focal Plane Array
GCPW	Grounded Co-planar Waveguide
GHz	Gigahertz ( $10^9$ Hz)
GRIN	GRadient-INdex
HDPE	High-Density Poly-Ethylene
HPBW	Half-Power Beam Width
IC	Integrated Circuit
ILA	Integrated Lens Antenna
IMLA	Integrated Metal-Lens Antenna
LNA	Low-Noise Amplifier

LOS	Line of Sight
LTCC	Low Temperature Co-fired Ceramics
M2M	Machine-to-Machine
MIMO	Multiple-Input Multiple-Output
mm-wave	millimeter-wave
MMIC	Monolithic Microwave Integrated Circuit
MSL	Microstrip Line
OEWG	Open-Ended Waveguide
PA	Power Amplifier
PAA	Phased Antenna Array
PCB	Printed Circuit Board
RF	Radio Frequency
S-parameters	Scattering parameters
SIW	Substrate-Integrated waveguide
SLL	Side Lobe Level
SP3T	Single-Pole three-Throw
SP4T	Single-Pole four-Throw
SPDT	Single-Pole double-Throw
TE	Transverse Electric
VM	Vector Modulator
VNA	Vector Network Analyser

## Symbols

$\Gamma$	reflection coefficient
$\epsilon_r$	relative permittivity
$\epsilon_{rm}$	effective relative permittivity of the parallel plates
$\eta_a$	aperture efficiency
$\eta_r$	radiation efficiency
$\eta_m$	matching efficiency
$\theta_{max}$	maximum steering angle
$\lambda$	wavelength
$\lambda_g$	wavelength in the dielectric medium
$\phi$	phase difference
$a$	separation between the parallel plates
$a_e$	major axis of the ellipse
$b_e$	minor axis of the ellipse

$A_p$	physical aperture area of the antenna
$d_a$	separation between array elements
$d$	diameter of the lens
$D$	directivity
$D_a$	maximum dimension of the antenna
$e$	eccentricity
$d$	separation between the array elements
$f$	focal length of the lens
$G$	antenna gain
$Gr$	antenna realized gain
$L$	length of the extension length
$L_p$	length of the patch
$P_{rad}$	power radiated by an antenna
$P_{acc}$	power accepted by an antenna
$R$	radius of the lens
$r_F$	far-field distance
$U_{max}$	maximum radiation intensity
$w_p$	width of the patch
$Z_a$	antenna impedance
$Z_s$	source impedance



# 1. Introduction

## 1.1 Introduction

Mobile communication systems have continued advancing since the early 1980s to provide ubiquitous service, support more subscribers, and improve the quality of service. A new generation of communication systems is launched almost every decade to improve data throughput and avoid network congestion [1]. The new generation of mobile communication systems, 5G, is currently in the deployment phase. The 5G network is planned to substantially improve data throughput, decrease latency, and facilitate machine-to-machine (M2M) communication [2]–[4]. The utilization of millimeter-wave frequencies, extreme network densification, massive MIMO, and cloud-based random-access technology are considered as the key enabling technologies [5].

Millimeter-wave frequencies are important due to the availability of large bandwidth for commercial applications [6]. The telecommunication standard development organization 3rd Generation Partnership Project (3GPP) has allocated K-band, 24.25-27.5 GHz, and V-band, 39.5-43.5 GHz, frequency ranges for random access network of 5G [7]. Countries such as China and Korea plan to utilize larger bands, that is 24.25-29.5 and 37-43.5 GHz. 5G also plans to utilize 10 GHz bandwidth available at E-band, 71-76/81-86 GHz, frequency range for wireless backhaul link to achieve throughput comparable to an optical fiber [8], [9]. Except for communication systems, millimeter wave technologies have ever-expanding scope in the field of automotive radar (77 GHz), security scanner, high definition video application (60 GHz) and many more [10], [11].

The atmospheric absorption and rain attenuation increase with the frequency [12], [13]. Therefore, at millimeter-wave frequency band, the electrical size of antennas should be larger to achieve high gain. The radiated beam of an electrically large antenna is narrow; therefore, the antennas with beam steering capability are preferred to cover a wide angular range. The phased antenna array is regarded as an ideal solution for high-gain with dynamic beam steering requirements [14]–[16]. However, with the higher gain requirement, the number



of array element increases and, consequently, the feeding loss/complexity and the number of active components (phase shifters, low noise amplifier, power amplifier) increase [17]. The large number of active components placed at the close interval causes significant heat dissipation per area, and the thermal management becomes critical [18]. Moreover, the cost of the antenna increases.

The beam-switching topology is an alternative solution for high gain requirements as it minimizes the number of feed lines and the active components required. The beam-switching architecture consists of a passive beamforming network, such as dielectric lens, reflector, planar Rotman lens, Butler matrix, etc., and radiating elements. The beam-switching topology generates a limited number of predefined beams based on the feed positions or configurations. The passive beam steering is less suitable for applications with changing environment, such as radio access link. In addition, RF switches used to enable the beam-switching network suffer from high insertion loss, approx. 2-3 dB per switch at mm-wave frequencies [19]. Furthermore, beamforming structures such as dielectric lenses are bulky, which makes them less desirable for commercial applications. This research work aims to improve the performance of the beam-switching antennas and make them viable for commercial applications.

## 1.2 Objective and impact

The research focuses on developing antenna solutions that meet the high gain, large beam-steering range, and wide bandwidth requirements of new-generation communication systems. Previous research identified beam-switching architecture as a potential solution. The work aims to:

- Design high-gain antennas at millimeter-wave frequency range with beam-switching topology.
- Reduce the form factor of the dielectric lens.
- Enable wide beam-steering range with low scan loss.
- Minimize the insertion losses of the beam-switching network.
- Investigate the possibility of dynamic beam steering and beamforming with the beam-switching antennas.

The research is done at the lower E-band frequency range, (i.e. 71-76 GHz), which can be potentially used for the point-to-point backhaul radio link. The wide beam-steering capability and beam-reconfigurability could make the beam-switching antennas suitable for the access links. The author believes that the efficient antenna solutions with reduced number of active components will minimize the cost and power consumption of the new generation of communication systems.

### 1.3 Scientific merits

The major scientific contributions of this dissertation are summarized as follows:

1. Design and characterization of high gain integrated lens antenna (ILA) operating at 71-76 GHz [I].
2. Focal length or form-factor reduction of an ILA:
  - Investigation of potential and challenges in using the high relative permittivity materials to reduce the focal length of an ILA [II].
  - Design, analysis and implementation of a low-profile integrated metal-plate lens (IMLA) based on combination of a dielectric ILA and metal-plate lens [IV][V].
3. Scan loss reduction of an ILA:
  - Implementation and characterization of an ILA with feeds on the spherical surface to minimize scan loss [III].
  - Design and implementation of the scan loss reduction technique for an ILA based on the radiation pattern tilting of the offset feeds along the focal plane [V].
4. Numerical study the ILA radiating properties with respect to varying mutual coupling and port impedance mismatch between the beam-switching array elements [VI].
5. Implementation of a beam-switching network with a high-gain vector modulator integrated circuit [VII]. Demonstration of the beam-reconfigurability of the beam-switching antenna.
6. Design and demonstration of the techniques to control the power coupled to series array radiating elements fed with substrate integrated waveguide [VIII].

### 1.4 Structure of dissertation

This thesis consists of an overview and eight publications. The overview section is divided into six chapters and provides the relevant background knowledge to the thesis, as well as, a brief summary and major outputs of the research work.

In Chapter 2, the essential antenna parameters are defined and the relevant literatures are reviewed. Chapter 2 also establishes the motivation for objectives set in this dissertation. Chapter 3 and 4 summarize the publications. Chapter 3 concentrates on the ILA and various methods implemented to decrease focal length and scan loss [I], [II], [III], [IV], and [V]. Chapter 4 focuses on the feed

network of the beam-switching antennas [VI], [VII], and [VIII]. Summaries of the publications are included in Chapter 5. Chapter 6 presents some conclusions based on the achieved results and discusses possible future work.

## 2. High gain antennas

This chapter discusses the basic antenna parameters that are most relevant to this thesis. In addition, the literature review of the antennas with potential to meet the requirements of 5G is presented and the recent developments in the relevant field are discussed.

### 2.1 Antenna parameter

Antennas are a means of transmitting and receiving radio waves [20]. An antenna transforms the alternating current in a transmission line into the electromagnetic (EM) waves in the free space and vice versa. An antenna is a typically passive and reciprocal device, in other words, the transmitting and receiving characteristics of the antenna are the same. As a single antenna cannot efficiently operate in the entire radio spectrum, an antenna is designed to operate at a specific frequency or range of frequencies known as operation bandwidth.

Based on the field distribution, the space around an antenna can be divided into the reactive near-field region, the radiating near-field region, and the far-field region. The region surrounding an antenna where the normalized radiation pattern is independent of the distance from the antenna is known as the far-field region. For an antenna with electrical size,  $D_a$ , comparable or larger than the wavelength, the far-field region is the space beyond the distance

$$r_F = \frac{2D_a^2}{\lambda} \quad (2.1)$$

from the antenna, where  $\lambda$  is the wavelength in free space. Most of the antenna radiation properties such as radiation pattern and directivity are measured in the far-field region. The radiation pattern is a graphical representation of the directional variation of the power radiated by an antenna. The normalized radiation patterns of an isotropic radiator and the 5-element array with half-wavelength separation are shown in Fig. 2.1 (a) and (b) with cartesian and polar plot, respectively. The radiation pattern helps to visualize important antenna parameters, such as the main lobe, half-power beam width (HPBW), side lobes,

and nulls. The main lobe or main beam is the lobe in the radiation pattern containing the highest power. The HPBW is the angular extent of the main lobe in which the magnitude of the radiation pattern is larger than 50% (or -3dB) of the peak power. Any lobe in a radiation pattern that is not the main lobe is a side lobe, and the side lobe in the opposite direction from the main lobe is called the back lobe. The radiation pattern also helps to visualize the directivity of an antenna.

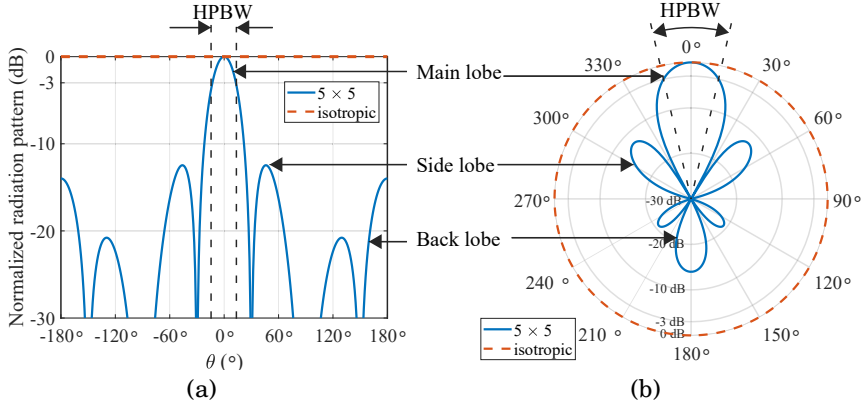


**Figure 2.1.** Azimuth cut of the normalized radiation pattern of an isotropic radiator and  $5 \times 5$  array with the element-separation distance of  $0.5\lambda$  in (a) cartesian and (b) polar coordinate system.

Directivity measures the ability of an antenna to focus the EM radiation toward a specific direction. Directivity is defined as the ratio of radiation intensity in any direction to average radiation intensity over all directions. The maximum directivity of an antenna is expressed as

$$D = \frac{4\pi U_{max}}{P_{rad}} \quad (2.2)$$

where,  $U_{max}$  is maximum radiation intensity (W/unit solid angle) and  $P_{rad}$  is the power radiated by the antenna. In the case of an isotropic antenna, the directivity is equal to 1 and higher directivity means the radiated power is focused in a narrower angular range.

The ratio of the radiation intensity of an antenna in a given direction to the radiation intensity of a isotropic antenna is known as the gain. The radiation intensity of the isotropic radiator is equal to the power accepted divided by  $4\pi r^2$  [20]. The maximum gain can be expressed as

$$G = \frac{4\pi U_{max}}{P_{acc}} = \eta_r D \quad (2.3)$$

where  $\eta_r$  is the radiation efficiency of the antenna, which is defined as the ratio of power radiated to power accepted, (i.e.  $\eta_r = P_{rad}/P_{acc}$ ). In an ideal case, for a lossless antenna with  $\eta_r = 1$ , the directivity and gain are equal. However, in practice, all the accepted power is not radiated, a fraction of power is dissipated, and, therefore,  $0 < \eta_r < 1$  and the gain is smaller than directivity.

The realized gain differs from the gain as it also considers the matching efficiency,  $\eta_m$ , in addition to the radiation efficiency  $\eta_r$ . The realized gain is expressed as

$$G_r = \eta_r \eta_m D. \quad (2.4)$$

The matching efficiency is expressed as  $\eta_m = 1 - |\Gamma|^2$ , where  $|\Gamma|$  is the reflection coefficient. The reflection coefficient is a parameter that describes the amount of EM wave reflected due to impedance mismatch [21]. Mathematically, the reflection coefficient,  $\Gamma$ , is expressed as

$$\Gamma = \frac{Z_a - Z_s}{Z_a + Z_s} \quad (2.5)$$

where  $Z_a$  and  $Z_s$  impedance of the antenna and RF source, respectively.

## 2.2 High-gain and beam-steering antennas

The antenna gain can be related to its physical aperture,  $A_p$ , aperture efficiency,  $\eta_{ap}$ , and radiation efficiency,  $\eta_r$ , as [22]

$$G = 4\pi \frac{A_p}{\lambda^2} \eta_{ap} \eta_r \quad (2.6)$$

The aperture efficiency,  $\eta_{ap}$ , is defined as the ratio of effective aperture to the physical aperture of an antenna. The aperture efficiency is the ability of an antenna aperture to convert available power into plane waves or vice versa.

The above equation states that the antenna gain can be improved by increasing  $A_p$ ,  $\eta_{ap}$ , and  $\eta_r$ . As the efficiencies, both  $\eta_{ap}$  and  $\eta_r$ , range between 0 and 1, the improvement in gain due to the efficiencies is limited. Therefore, significant gain improvement can only be achieved by increasing the physical aperture of an antenna. With increasing gain, the beamwidth becomes narrower. Therefore, beam-steering capability is favoured to achieve wide angular coverage.

A parabolic reflector antenna mounted on the gimbal or rotator has been popularly used in radio astronomy, satellite communication, and point-to-point radiolink applications to achieve high gain and beam steering [23], [24]. The mechanical steering is slow and requires significant volume [23]. The availability of phase shifters, power amplifiers, and RF switch MMICs has facilitated the implementation of electronic beamsteering. The phased array antenna, integrated lens antenna, reflectarray, transmitarray and leaky-wave antenna have been popular choices for applications requiring high-gain and beam-steering antennas [17], [25]–[28].

### 2.2.1 Phased array antenna

An antenna array is a group of two or more simultaneously radiating elements arranged in a geometrical grid. An array can also be regarded as the discretization of a large aperture into smaller radiating elements whose excitation amplitude

and phase can be controlled. The radiation pattern of an array is calculated by adding the radiation pattern of individual radiating elements [20]. The control over the excitation amplitude and phase of the radiating elements enable constructive or destructive summation of the fields to the desired directions, and beam steering is implemented. The directivity of an array is proportional to the number of array elements, the distance between the array elements, and element directivity. To avoid grating lobes in the radiation pattern, the separation distance  $d_a$  between the array elements should be

$$d_a < \frac{\lambda}{1 + \sin(\theta_{max})} \quad (2.7)$$

where,  $\theta_{max}$  is the maximum steering angle of the array [29]. Typically, the array elements are separated by approx.  $\lambda/2$  distance to achieve a wide steering range without the grating lobe. The steering angle of an array is determined by the phase difference between the array elements. Ideally, there is no limit to the beam steering range of a phased array. However, in practice, the non-ideal element pattern and mutual coupling between the array elements limit the steering range.

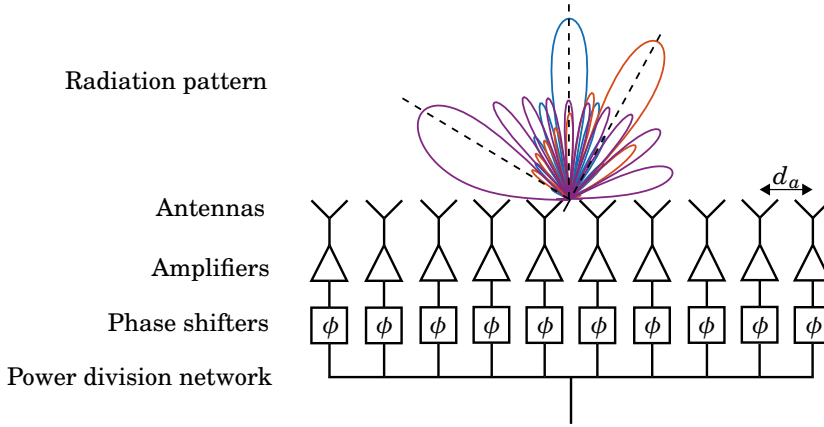


**Figure 2.2.** Schematic diagram and radiation patterns of a 10-element phased array with  $d_a = \lambda/2$  and cosine-type element pattern.

Generally, the phased antenna arrays are implemented on a printed circuit boards (PCB) due to ease in the integration of the active components [14], [30], [31]. A microstrip patch antenna is a popular choice as a radiating element for PCB-based arrays. The multi-channel beamforming chips are used to control the excitation of array elements [31]–[33]. The beamforming chips consist of a phase shifter and variable gain amplifier in each channel. For example, the beamformer chip in [30] can provide upto 25 dB of amplitude control and  $360^\circ$  phase control with approx.  $5.6^\circ$  steps. The phase shifter resolution of  $5^\circ$  provides the beam-steering resolution of  $1.4^\circ$  with the progressive phase shift across the  $8 \times 8$  array [34]. The beam steering resolution can be further improved with the non-uniform phase gradient across the radiating elements. In addition, the

vector modulator MMICs are also used that give upto 30 dB amplitude and 360° phase control [35].

In [36], an array of 1024 elements is designed to meet the requirements of Ku-band satellite communication systems. A  $16 \times 16$  array is designed by combining  $4 \times 4$  phased array modules to achieve 28.8 dB directivity and a beam steering range of  $\pm 70^\circ$  in both azimuth and elevation planes. The PAA can also be used to tailor the radiation pattern [14]. The  $8 \times 8$  Vivaldi array demonstrates the dual-polarized operation at the Ka-band and steers the main beam to  $\pm 60^\circ$  with a 3 dB scan loss [37].

As the number of array elements increases, the transmission line losses and the number of active components, (i.e. phase shifters, low noise amplifiers [LNA], and power amplifiers [PA]), also increase. The transmission line losses can be minimized by using low loss transmission lines, such as waveguides or substrate integrated waveguides (SIW) [38], [39]. Most of the power consumed by active components is dissipated as heat, therefore, a cooling system is essential [18]. A higher number of active components also lead to an increase in the cost.

### 2.2.2 Beam-switching antennas

A beam-switching antenna (BSA) is the combination of a passive beamforming network (BFN) and radiating elements. A passive BFN is a multi-input and multi-output network that generates unique amplitude and phase distribution across its output ports for each input port. As the single input port of a BFN can excite many radiating elements, a high gain can be achieved with lower feed complexity. Typically, the input ports of BFN are designed or positioned to steer the main beam in different directions to achieve beamsteering. Typically, only one input port of the BFN is connected with the RF source at a time. The input port selection of a BFN is done with a network of RF switches, known as a beam-switching network (BSN). The BSAs are popular in applications that require high gain and narrow beam steering ranges. In comparison to the PAA, illustrated in Fig. 2.2, the BSA in Fig. 2.3 can achieve a similar gain with lower feed lines and active components.

The number of input ports of a BFN equals the number of beams generated by the BSA. The passive beam steering or generation of limited predefined beams is considered as a major drawback of the BSA. Generation of the reconfigurable beams with BSA has been demonstrated in [40], [41]. The BSA in both works is based on the concept of simultaneous excitation of multiple input ports of the passive BSN. The publication [VII] presents a solution to generate reconfigurable beams with BSA.

An electronic BSN is implemented with the RF switches [42], [43]. In OFF state, an RF switch provides better isolation than -25 dB [44]. The insertion loss of a RF switch ranges between 2-3 dB at millimeter-wave (mm-wave) frequency [19]. With an increasing number of feed lines, the RF-switches are arranged in cascade connection and the total insertion loss is the sum of insertion loss



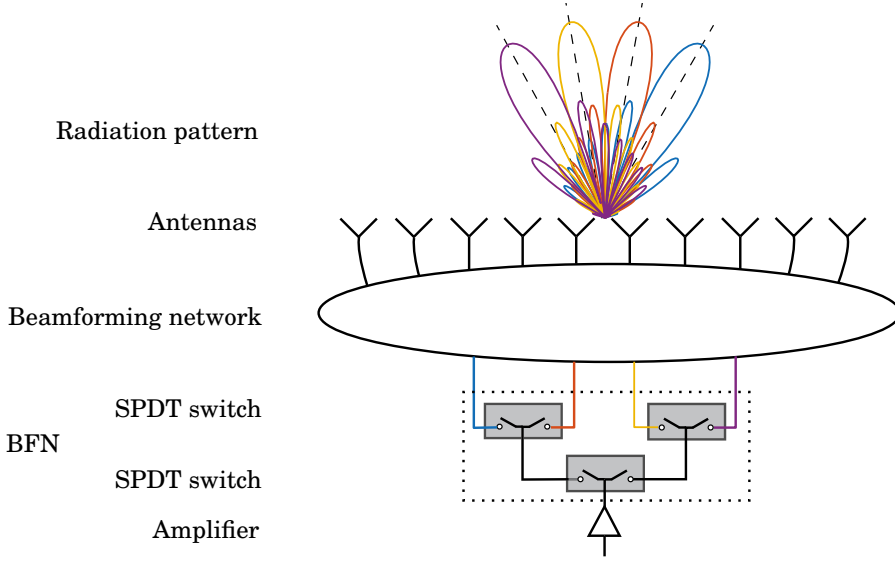


**Figure 2.3.** Schematic layout and radiation patterns of a BSA consisting of a passive BFN with four input ports and 10 radiating elements.

at each stage. The BSN for an array of 64 antennas is implemented with four layers of cascaded SP4T switches in [45]. The total insertion loss in the BSN is approx 15 dB. In [46], the insertion loss of the BSN designed with two layers of cascaded SP4T switches is 6.5 dB. In Publication [VII], the RF switch is replaced with the high-gain vector modulator IC in the BSN to minimize the insertion loss.

The Rotman lens, Butler matrix, Nolen matrix, and Blass matrix are commonly used BFNs for applications requiring high-gain and beam-steering antennas [47]–[50]. Generally, the output ports of the BFN are connected to an array of radiating elements to generate a directive beam [43], [51]. The above-mentioned BFNs are used to excite linear arrays. As a result, the beam is steered along one dimension. 2D beamsteering has been implemented with planar BFN using the frequency-steering series array [52]. The excitation phase of the series-array elements changes with the frequency, thereby steering the beam along the axis of series array. An axially symmetric 3D lens antenna that operates based on the beam-switching topology enables the 2D beamsteering and attains high gain [53], [54]. The dielectric lens antennas are discussed in the next section.

## 2.3 Integrated lens antenna

A lens is a transmissive, shaped dielectric structure that focuses or collimates the spherical wavefront. The use of dielectric lenses to collimate the radiation at microwave frequency can be dated back to the late 19th century [55], [56]. The operation of a lens can be understood by the principle of refraction and reflections.

Based on the positioning of the feed, a lens antenna can be categorized into an off-body fed lens and integrated lens antenna (ILA) [57]. A lens with the feed antennas in direct contact with the lens body is defined as an ILA. An ILA helps to minimize the substrate modes of the planar feed antennas and increase the directivity of the feeds [58]. A simplified 2D diagram of an ILA is presented in Fig. 2.4. Based on the shape of the collimating surface, the ILA can be further categorized as an elliptical or hemispherical ILA.

### 2.3.1 Design

The design and operation of elliptical and hemispherical ILAs are detailed in [53] and [59], respectively. As shown in Fig. 2.4, the length of the extension section,  $L_{ell}$ , of an elliptical ILA is calculated as

$$L_{ell} = e \cdot a_e, \text{ where } e = \frac{1}{\sqrt{\epsilon_r}} = \sqrt{1 - \left(\frac{b_e}{a_e}\right)^2} \quad (2.8)$$

In the above equation,  $e$  is the eccentricity of the elliptical ILA,  $\epsilon_r$  is the relative permittivity,  $a_e$  is the major axis and  $b_e$  is the minor axis of the ellipse. The focal length of the elliptical ILA  $f = a_e + L_{ell}$ . The extension length of the hemispherical ILA,  $L_{hem}$ , can be estimated with

$$L_{hem} = R \frac{1}{\sqrt{2}} \frac{\epsilon_r}{\epsilon_r - 1} \quad (2.9)$$

where  $R$  is the lens radius of the ILA [59]. The focal length of the hemispherical ILA  $f = R + L_{hem}$ . For the elliptical and hemispherical ILA, the shape and focal length depend on the  $\epsilon_r$ . The aperture efficiency of an optimized elliptical and hemispherical ILA is greater than 90% and 80%, respectively [60]. To achieve optimal directivity, the focal length criteria must be met, which makes an ILA bulky. However, a shorter focal length would make an ILA aesthetically pleasing for commercial applications.

Over the years, the ILA has been designed to improve the gain, steer the main beam, and generate the tailored or multi-beam radiation patterns [45], [61]–[63]. The computer numerical control milling machine (CNC) and injection moulding are the most commonly used manufacturing processes of an ILA. A CNC can achieve upto 50  $\mu\text{m}$  accuracy [57]. The injection moulding method can be specially effective to fabricate multi-material ILAs [64]. Recently, 3D-printing technology has assisted in prototyping the ILA at mm-wave and sub-THz frequencies [65], [66]. The geometric optics (GO) and physical optics (PO) methods are widely used to simulate the ILA radiation pattern at high frequencies. The GO/PO simulations provide good accuracy in a short time compared to the full-wave simulation methods [67].

The losses in an ILA can be categorized into: spillover, reflection and dielectric loss [68]. The field incident and exiting from the extension section of the ILA is not collimated towards the desired direction, it distorts the ILA radiation

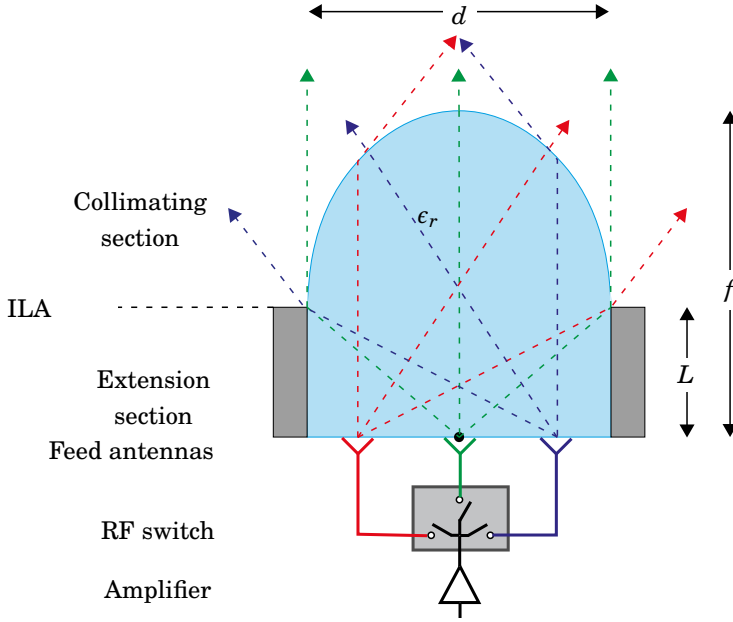


**Figure 2.4.** Schematic diagram of an elliptical ILA with BSN illustrating beam steering.

pattern and decreases the directivity. In practice, the absorbers are placed along the extension section to prevent RF power leaking from the extension section. In ray-tracing simulations, the field incident on the extension section is not considered during far-field calculation and it is regarded as the spillover loss [69].

The impedance difference at the ILA and free space boundary lead to the reflections. The reflected field eventually exits from the lens after multiple reflections, either through collimating surface towards undesired direction or from the extension section into the absorber. In case of low permittivity materials, with  $\epsilon_r < 4$ , the reflected rays have minimal effect on the ILA radiation pattern [70]. In ray-tracing simulations, the reflected fields are not considered in far-field calculation, but rather categorized as loss [67], [68]. The reflection loss of an ILA depends on the shape of the collimating surface and the  $\epsilon_r$  of the ILA [71]. The internal reflections in an ILA can be minimized using a quarter-wavelength matching layer in the collimating surface [72], [73]. The reflection loss of an elliptical ILA can be decreased by making the minor axis is larger than the radius [68]. However, the larger minor axis increase the extension length, thereby increasing the spillover loss and reducing the gain. A fraction of EM energy radiated by the feed is dissipated in the ILA. The dissipation loss is proportional to the loss tangent,  $\tan\delta$ , and the volume of the ILA. An analysis of the losses demonstrates that a shorter focal length will help to minimize the spillover loss and dielectric loss, thereby making it possible to design efficient ILAs.

The design equations of an elliptical and hemispherical ILA show that the focal length can be reduced by using materials with higher relative permittivity. The

focal length to diameter ratio,  $f/d$  for a Teflon ( $\epsilon_r = 2.1$ ), quartz ( $\epsilon_r = 3.7$ ), and silicon ( $\epsilon_r = 11.7$ ) material are 1.15, 0.87, and 0.68, respectively [67], [74], [75]. The high permittivity materials are usually lossy, rare, expensive, and difficult to shape which makes them less suitable for mass manufacturing. Furthermore, the high permittivity materials suffers from high internal reflections and the matching layer is required. The gradient index lens (GRIN) and multi-material lenses are also designed to reduce the focal length [76], [77]. The fabrication of GRIN lenses with a periodic subwavelength structure is challenging at mm-wave frequencies. Moreover, the efficiency of the GRIN is lower than the homogenous ILA [78], [79]. A multi-material ILA is designed in [77] with the MACOR  $\epsilon_r = 5.5$ , and acrylic,  $\epsilon_r = 2.53$ , materials attains the  $f/d$  ratio of 0.78. The radiation efficiency of the double-shell ILA is approx.  $-6.2$  dB which is mostly due to higher dielectric loss in the MACOR and acrylic.

In [80] and [81], the air cavity along the feeding plane reduced the focal length of a hemispherical ILA to reduce the focal length and weight. An approximately 50% reduction in the height of the 120-mm elliptical ILA is achieved by using the  $2 \times 2$  array of ILA with 60 mm diameter [82]. However, the complexity in the feed network also increases as the number of feed element increase from one to four. A compact lens based on the folded Fresnel zone plate is designed to operate at V-band and achieved the  $f/d$  of 0.22 [83]. The radiation efficiency of the antenna ranges between 34 and 53 %. While the above literature provides significant improvement in the ILA  $f/d$  ratio [80]–[83], the beam steering properties of the lenses are not discussed.

### 2.3.2 Scan loss

The main beam of an ILA can be steered by changing the position of the feed antenna along the focal arch or focal plane as shown in Fig. 2.4. In practice, an array of feed antennas is positioned along the focal plane of the ILA and a single feed is excited by an electronic BSN [25], [45]. As the main beam is steered away from the boresight or the feed is located away from the focal center, the gain of an ILA decreases. The reduction in gain with respect to the steering angle is termed scan loss. In the case of an ILA, the increase in scan loss is caused by the following factors:

- Reduction in effective aperture with increasing steering angle.
- Decrease in radiating aperture due to increase in total reflections as the feed antenna move away from the focal center.
- Increase in spillover loss at larger feed offset position.
- Non-uniform amplitude and phase distribution across the ILA aperture when the feed is at larger offset position from the focal center. Typically, the main beam of feed antenna is directed towards the edge of the ILA radiating aperture. Illustrated by red curve in Fig. 2.5.

- Aberration (i.e. the distortion of phase pattern at the ILA aperture) caused by offset in feed position between the ideal focal arch and focal plane.

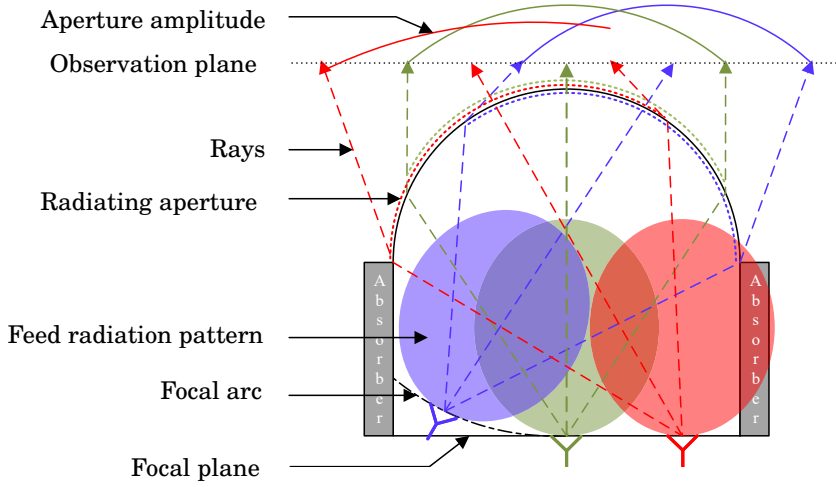


**Figure 2.5.** Schematics diagram illustrating the scan loss sources of an extended hemispherical ILA when the feeds are positioned along the focal plane and focal arc.

An ILA with a shaped collimating surface is designed to combat the decrease in the effective radiating aperture with increasing steering angle [84]. The simulation study in [60] shows that the elliptical ILA with collimating surface eccentricity of  $0.78/\sqrt{\epsilon_r}$  gives optimal beam steering performance for a  $25^\circ$  steering angle in comparison to the eccentricity of  $1/\sqrt{\epsilon_r}$ . In [85], the extension length of the extended hemispherical lens is reduced by  $0.6\lambda_0$  at 28 GHz to limit the scan loss below 1 dB at a  $30^\circ$  steering angle. In both the above-mentioned works [60], [85], the boresight directivity is compromised to minimize the scan loss.

The aberration of the hemispherical ILA is minimized by using the double lens system with  $1.05 f/d$ , which limits the scan loss below 1.2 dB for a  $30^\circ$  steering angle [86]. Similarly, a dual-lens system with  $2.24 f/d$  is designed to minimize the scan loss below 2 dB upto a  $50^\circ$  steering angle at 500 GHz [87]. The aberration of the GRIN lens and the dielectric dome lens is minimized by feeding the lenses with the phased array antenna, which extends the scanning range of the lens to  $\pm 60^\circ$  and  $\pm 70^\circ$ , respectively [79], [88].

The aberration is also minimized by positioning the feed along the focal arch rather than the focal plane [89]. The design of the homogenous dielectric lens with negligible aberration by placing the feeds along the spherical surface is presented in [59]. An extended hemispherical ILA is designed and manufactured from Teflon to steer the main beam to  $\pm 30^\circ$  [90]. The feed elements are positioned along the spherical surface to limit scan loss below 1 dB. The positioning of the feeds along the focal arch also helps to minimize the spillover loss and improve the amplitude distribution in the ILA radiating aperture, as shown in Fig. 2.5.

GRIN lenses, especially the Luneburg lens, are suitable for the wide beam scanning application [91]. A flat Luneburg lens with ultrawide 1D-beamsteering capability has been demonstrated with various materials and techniques [92]–[95]. For both homogeneous and GRIN lenses with the spherical feed surface, designing feeding system for 2D-beamsteering is a challenge.

The off-axis reception performance of the silicon-ILA, used in an imaging application, is improved by tilting the radiation pattern of the double-slot feed antenna at the offset position. The feed pattern tilting improved reception from a  $45^\circ$  angle by more than 5 dB [96].

### 2.3.3 Area of focal plane array

The relation between  $f/d$  and the area of the focal plane array (FPA) of an elliptical ILA is discussed in this section. The  $f/d$  of an elliptical ILA is a function of relative permittivity, as explained in Section 2.3.1. Based on Snell's law, for a given steering angle,  $\theta_s$ , the offset feed position and the area of FPA is proportional to  $f/d$ .

Fig. 2.6 shows that the FPA area is significantly smaller than the radiating aperture area when the maximum steering angle,  $\theta_s$  is small. With increasing  $f/d$  and  $\theta_s$ , the FPA area increase. It is not practical to steer the main beam to wider angles with an ILA of larger  $f/d$ . For example, when  $\theta_s = 40^\circ$ , using an ILA with an  $f/d$  greater than 1.08 will result in an FPA area larger than the actual radiating area, which is not efficient and practical. In practice, the FPA area needs to be a fraction of the actual radiating area. In [97], the silicon-ILAs with 0.63  $f/d$  steered the main beam to  $\pm 60^\circ$  with an FPA area equal to a quarter of the radiating aperture area. The small FPA area could result in fewer feed elements, fewer active components, and lower transmission line loss, and vice versa. It should be noted that the lower  $f/d$  is not a sufficient condition to achieve larger steering angle, the ILA off-axis properties are also significant.

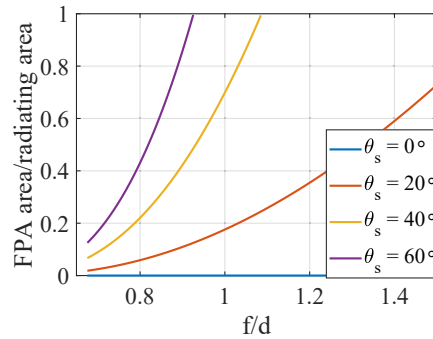


**Figure 2.6.** Ratio of the FPA area to radiating aperture area of an elliptical ILA w.r.t.  $f/d$  for varying steering angles,  $\theta_s$  when  $d = 16\lambda$ . The scan loss of the elliptical ILA is not considered during the calculations.

The ILAs with low  $f/d$  have lower losses, enable wide beam steering with fewer active components, and dimension and weight reduction make it more

appealing for commercial applications. Therefore, the publications [II], [IV], and [V] are aimed towards minimizing the  $f/d$  of an ILA.

The number of FPA elements is determined by the maximum beam-steering angle,  $\theta_s$ , beam cross-over criteria,  $f/d$  of the ILA, and the minimum dimension of the single FPA radiating element. As mentioned in previous paragraph, the maximum steering angle,  $\theta_s$ , and  $f/d$  of the ILA determine the FPA area. The density of the FPA radiating elements is determined by the beam cross-over level criteria. Most beam-steering applications require high beam cross-over level, typically  $-3$  dB, to provide continuous coverage. Higher beam cross-over criteria and smaller  $f/d$  of the ILA lead to smaller interval between the FPA elements [68]. However, the minimum possible separation distance is determined by the dimensions of the FPA radiating elements. When the FPA elements are placed in close interval the coupling increases. The effect of closely positioned FPA elements on the ILA performance is studied in [VI]. A potential solution to improve the beam cross-over level of the beam-switching antenna with sparsely positioned FPA elements is discussed in [VII].

## 2.4 Antenna design

In general, the antenna design process starts with an objective or objectives, which is followed by the study of relevant theories and previous works. Based on the studies, a suitable antenna solution is proposed. The proposed antenna is simulated and tuned to meet the objectives. The fabrication method and its requirements are considered during the design and simulation phase. Finally, the antenna is fabricated and measured to verify the achievement of the objectives.

### 2.4.1 Design and simulation

The EM simulations ease and expedite the RF design process and also help to achieve desired results with fewer prototypes. The EM simulators allow to test the ideas, estimate the properties of antennas and tune antenna designs before building the prototype.

The dielectric ILAs presented in [I], [II], and [VI] are simulated with the in-house MATLAB-based ray-tracing software. The far-field radiation pattern of the feed antenna, simulated with the full-wave simulator, is used as the source in ray-tracing simulations. The ray optics based simulator offers good accuracy for a short computation time.

The simulations of more complex structure such as [IV], [IV], [VII], and [VIII] are done with the commercial full-wave simulator, CST Microwave Studio. The Computer-aided design (CAD) feature together with the various EM solver, such as the time domain and frequency domain solver, makes the simulator suitable for analyzing the complex structures.

### 2.4.2 Measurement

The measurements of an antenna ensure that the properties such as impedance, bandwidth, radiation pattern, gain, and polarization behave as designed and meet the specifications and regulations. The impedance and coupling properties of an antenna are verified with the scattering (S-) parameter measurements. In addition, the S-parameter measurement determines the impedance bandwidth of the antenna. The S-parameters are measured using a vector network analyzer (VNA) that operates at the suitable frequency range. The calibration of the VNA before an S-parameter measurement is essential to achieve the correct results.

The thesis deals with the electrically-large high-gain antennas, therefore, the properties such as radiation pattern, gain, and polarization are measured with the planar near-field measurement technique. The planar near-field measurement requires small space as compared to the far-field measurement. In a planar near-field measurement, the radiated fields are measured in a rectangular grid in the radiating near-field zone of the antenna under test (AUT). The far-field is calculated by Fourier transformation of the measured near-field and applying the probe compensation. In the thesis, all the near-field measurements and far-field calculations are done with NSI 200V 5×5 scanner and NSI-2000 software, available at Aalto University. The gain of an AUT is estimated with the gain comparison method. A reference antenna of known gain and the AUT are measured with the same setup and their peak amplitudes are compared to estimate the AUT gain.

The measured near-field data can be numerically transformed into the radiating aperture fields or holograms. The radiating aperture fields are numerically calculated with Fourier transformation-based back-propagation of the measured near-field data [98]. The feature is frequently used to verify the AUT operation and diagnose the potential faults [V], [VII], and [VIII].





### 3. Low-profile and low scan loss integrated lens antenna

#### 3.1 Introduction

The new generation of communication system, 5G, is adopting the mm-wave frequency for access links and for back-haul the E-band (i.e. 71-76/81-86 GHz) is taken in to use to complement currently used e.g. the 32, 38, and 58-60 bands [99]. In the backhaul radio links, the transmitting and receiving antennas are fixed, in line of sight (LOS), and the link distance is larger [8]. Therefore, the antennas need to have high-gain and narrow beam steering range. The high gain antennas increase the hop length and maximize the data throughput [100]. The beam steering capability combats the accidental misalignment of the antennas. As discussed in Section 2.2.2, the beam-switching antenna can provide high gain with a limited number of feed lines. The ILA-based BSA has been implemented for the point-to-point radio link [42], [45], [101].

The operation scenario is different in the radio access link. User equipment functions at closer distances, constantly moving and the background is changing. The access link antennas at the base stations need more than a 20 dBi gain and a wide beam steering range, approx.  $\pm 60^\circ$ , especially along the azimuth direction [15], [16]. Dynamic beamforming that gives control over the directivity, beamwidth and main beam angle of the radiation pattern is important to operate in an ever-changing environment [14]. The PAA has been widely adopted for the 5G radio access link as it meets most requirements [14], [15], [30], [33]. In general, in a 28-GHz 5G access network, the phased array antenna with 64 elements has been implemented to achieve directivity around 23.2 dB [34].

The mm-wave massive MIMO is regarded as an enabling technology for 5G [102], [103]. Accordingly, the access link antennas need to support mm-wave massive MIMO. Implementation of mm-wave massive MIMO with PAA requires exceptionally high transceiver complexity. Recent studies showed that the implementation of mm-wave massive MIMO with dielectric lens improves the performance and reduces the transceiver complexity and cost [104], [105]. The dielectric lenses for massive MIMO operations are expected to achieve wide

angular coverage.

The possibility to achieve high gain with a reduced number of feed lines is a major advantage of an ILA. However, the ILA beamsteering range is inherently narrow and scan loss is high which makes it less suitable for the radio access link. Various ILA solutions are presented in [II], [III], and [V] to enable a wide steering range with minimum scan loss. As discussed in Section 2.3.3, an ILA with smaller a  $f/d$  enables wide beam steering with less feed lines. Furthermore, the ILAs with shorter  $f/d$  also save volume and are aesthetically pleasing. Therefore, ILA designs to achieve high gain, minimize  $f/d$  ratio, and improve efficiency are presented in [I], [II], [IV], and [V]. All the ILA prototypes are designed to operate at the lower E-band, 71-76 GHz, dedicated to communications. However, many developed solutions can be adapted for lower frequency bands.

### 3.2 Integrated lens antenna for backhaul application

An integrated lens antenna (ILA) is designed, fabricated and characterized to meet the European Telecommunications Standards Institute (ETSI) regulations for the point-to-point antenna for fixed radio systems operating at the frequency range of 66 - 86 GHz [I]. The regulation stipulates that the minimum nominal antenna gain greater than 38 dBi and the beam steering range of  $\pm 5^\circ$  [106]. An in-house MATLAB-based ray-tracing software is used to simulate the ILA performance.

The simulation study suggested that materials with the relative permittivity,  $\epsilon_r$ , between 4 and 5 are suitable for the optimum gain performance of the ILA (see Fig. 3.1). However, it is difficult to find materials with a low loss tangent,  $\tan\delta$ , at the above-mentioned  $\epsilon_r$  range that are suitable for mass manufacturing.

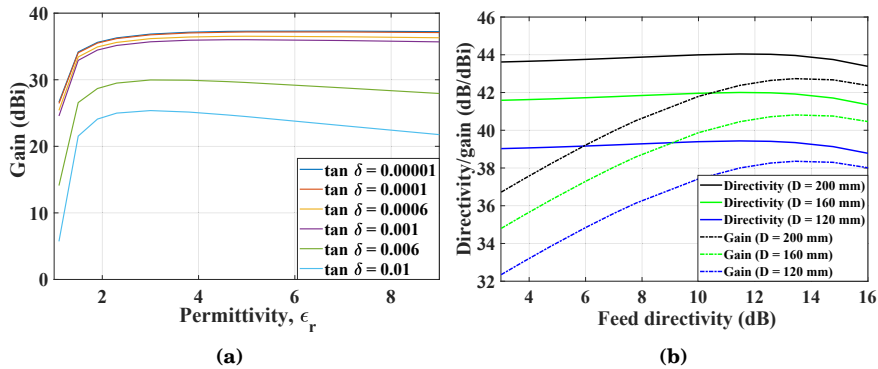


**Figure 3.1.** (a) Gain variation of the 120-mm elliptical ILA with varying permittivity,  $\epsilon_r$ , when fed by the WR-10 OEWG with 8.27-dB directivity and (b) directivity and gain of the HDPE-based elliptical ILA as a function of the feed directivity at 73.5 GHz. Reprinted from [I].

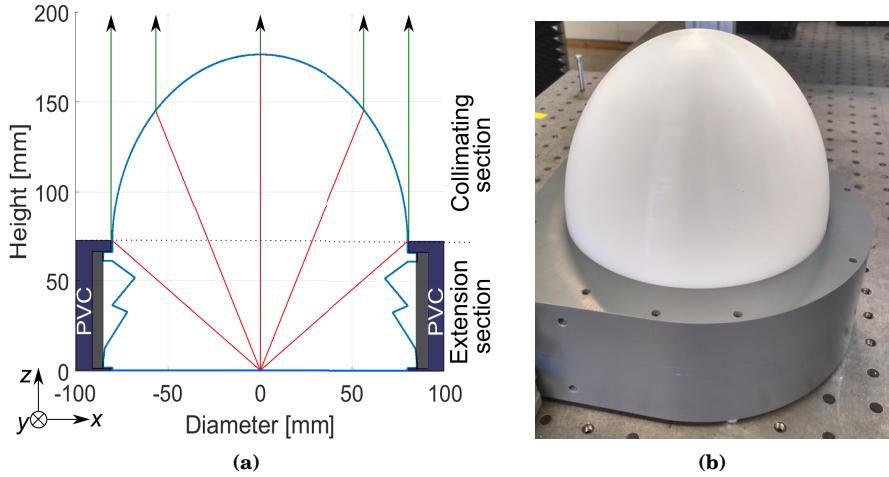


**Figure 3.2.** (a) 2D shape and (b) fabricated 160-mm ILA with the supporting PVC structure. Reprinted from [1].

The High-Density Polyethylene (HDPE),  $\epsilon_r = 2.31$ ,  $\tan\delta = 0.0002$ , material is chosen for ILA design, primarily due to its low  $\tan\delta$  [107]. In addition, the density of the HDPE, which is  $0.97 \text{ g/cm}^3$ , is lowest among the dielectric material used for an ILA design which helps to minimize the weight.

The efficiency of the ILA can be improved by optimizing the feed directivity. The simulation study of the elliptical ILA of Polyethylen material illustrates that the feed directivity of 13-14 dB provides the maximum ILA boresight gain (see Fig. 3.1 [b]). The directive feed significantly decreases the spillover loss and the reflection loss decreases marginally. The radiation pattern of a WR-10 open-ended waveguide (OEWG) with 8.27 dB directivity is used as the source in the ray-tracing simulations.

The ILA diameter of 160 mm is selected to achieve a minimum 38-dBi gain towards the boresight. The length of the extension and collimating section are 66.2 mm and 110.2 mm, respectively. The total height of the lens is 176.4 mm and the focal length to diameter ratio,  $f/d$ , is 1.1, as shown in Fig. 3.2 (a). Fig. 3.2 (b) shows the fabricated ILA with PVC support structure.

The simulated directivity of the ILA is 41.8 dB and the total loss is 3.55 dB. The spillover, reflection, and dielectric losses are 1.8, 1.3, and 0.45 dB, respectively. The simulated and measured gain of the ILA fed with the WR-10 waveguide are 38.23 dBi and 38.85 dBi, respectively, as shown in Fig. 3.3. The measured HPBW and SLL of the ILA are  $1.4^\circ$  and -17.77 dB, respectively. Both, the simulation and measured radiation patterns comply with the radiation pattern envelope (RPE) regulation of the ETSI. At  $\theta > 60^\circ$ , the SLL is higher than the RPE. The reflections from the outer edge of the collimating surface might be a potential source of higher SLL. The main beam is steered to  $5^\circ$  by displacing the feed to a 9.2 mm offset position from the focal center. The simulated and measured scan loss are 1.52 dB and 2.3 dB, respectively.

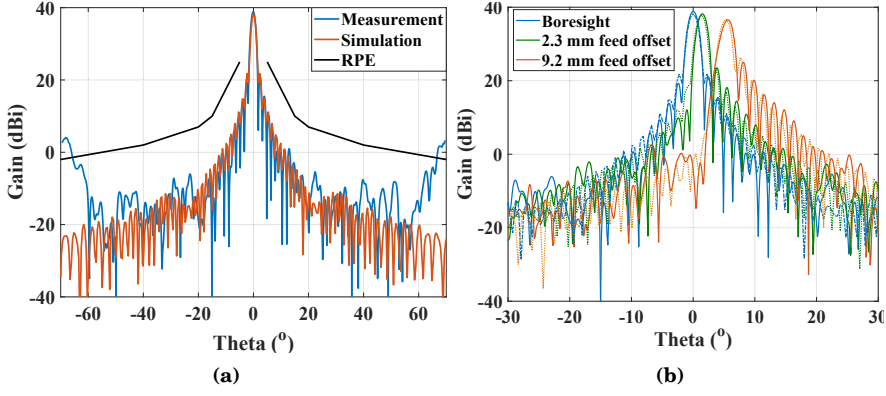


**Figure 3.3.** Comparison between the measured (—) and simulated (—) radiation patterns of the 160-mm lens at (a) bore-sight and (b) few beamsteering angles. Black curve in (a) is radiation pattern envelope (RPE) by ETSI for antennas used for point-to-point radio link at 71-86 GHz. Reprinted from [I].

Based on the simulation results presented in Fig. 3.1, the WR-10 OEWG directivity of 8.3 dB is not optimal of the ILA gain. Fig. 3.4 (a) demonstrates a stacked aperture coupled microstrip patch antenna (ACMPA) feed with 11.1 dB directivity is designed to improve the gain performance of the ILA. The simulation study shows that the bore-sight gain improves by approx. 2 dB compared to WR-10 OEWG feed (see Fig. 3.4 [b]). The scan loss at  $5^\circ$  steering angle improves by 0.7 dB with the stacked ACMPA feed. When the stacked ACMPA is surrounded of identical elements, the feed directivity is 9.6 dB and the ILA gain improves by 1.3 dB compared to WR-10 OEWG feed.

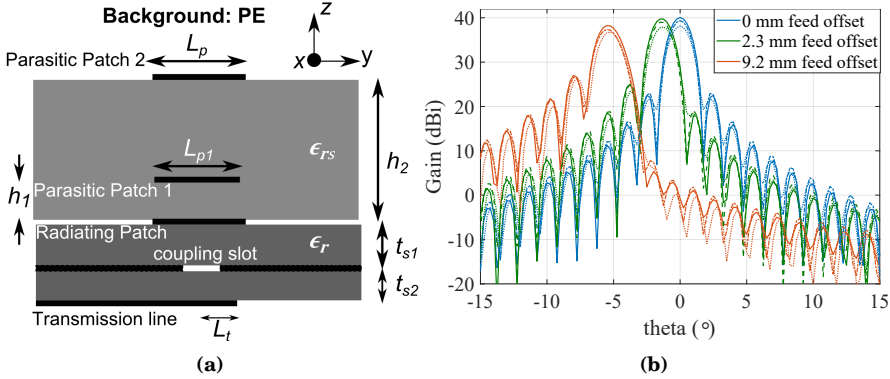


**Figure 3.4.** (a) Side view of an isolated stacked ACMPA feed antenna and (b) radiation pattern comparison of the ILA with waveguide (· · ·), stacked ACMPA with surrounding identical elements (—) and isolated stacked ACMPA (—) feeds. Reprinted from [I].

This work demonstrates that the traditional dielectric ILA can achieve high-gain and a narrow beam-steering range with fewer radiating elements compared to a PAA. Furthermore, it highlights that the ILA is bulky,  $f/d = 1.1$ , losses are substantial, 3.55 dB, and the scan loss is significant, 2.3 dB at a  $5^\circ$  steering

angle. The remainder of the chapter focuses on various techniques to improve the traditional ILA.

### 3.3 Effect of material properties

In [II], we aim to understand the benefits and disadvantages of using a high  $\epsilon_r$  material for ILA design. Two ILAs are designed with Rexolite ( $\epsilon_r = 2.53$ ,  $\tan\delta = 0.0013$ ) and PREPERM L450 ( $\epsilon_r = 5.01$ ,  $\tan\delta = 0.0046$ ) materials. The dimensions and far-field properties of the ILAs are compared to demonstrate the effect of material properties.

The ILAs with higher  $\epsilon_r$  reduces the height or focal length of an ILA (see Fig. 3.5 [a]). With increasing  $\epsilon_r$  and fixed  $\tan\delta = 0.0006$ , the length of the extension section and the spillover loss decrease. However, the higher  $\epsilon_r$  material usually have higher  $\tan\delta$  or are rare, difficult and expensive for mass production. Since, the dielectric loss of an ILA is proportional to  $\tan\delta$  and volume of the ILA, the lossy dielectric material is not an ideal choice for the high gain or large ILA design. A representative example is shown in Fig. 3.5 (b), where elliptical ILAs with the L450 material are simulated with diameters ranging from 100 to 300 mm. The directivity of the L450-ILA is proportional to its diameter, however, the gain decreases after the diameter exceeds 200 mm which is due to excessive dissipation loss.

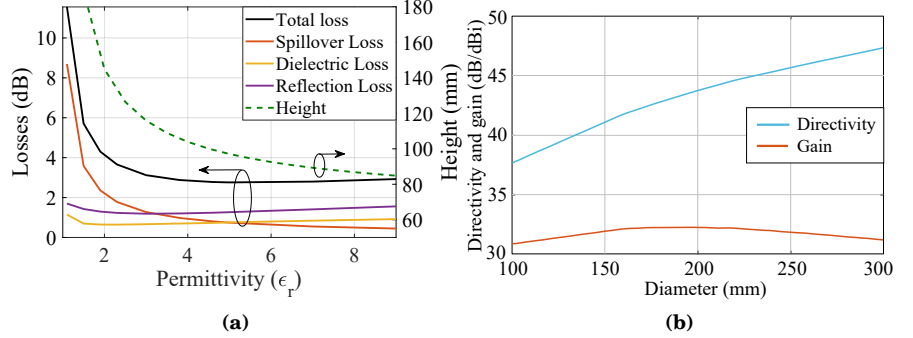


**Figure 3.5.** (a) The losses and height variation of the 120-mm ILA w.r.t.  $\epsilon_r$ , for constant  $\tan\delta = 0.0006$ , and (b) simulated gain and directivity variation of the L450-ILA ( $\epsilon_r = 5.01$ ,  $\tan\delta = 0.0046$ ) w.r.t. diameter. Reprinted from [II].

The 2D cross-section of the designed ILAs and fabricated ILAs are shown in Fig. 3.6 (a) and (b), respectively. Both designed ILAs have a radius  $R$  of 32 mm. The  $f/d$  of the Rexolite and L450 ILAs are 1.13 and 0.88, respectively. The collimating surface of both ILAs is designed with a minor axis of the ellipse,  $b_e = 1.1 \times R$  to minimize the internal reflections and scan loss [68]. The radius smaller than the minor axis minimizes the reflection at the edges of the collimating surface, which helps to avoid high SLL at larger angles, as shown in measurement results of [I]. Furthermore, the larger minor axis of collimating surface also minimizes the

reflections when the feeds are at offset positions, which leads to improved beam steering performance. The ILAs are studied with ray-tracing simulations and the radiation pattern of the WR-10 waveguide is used as the feed.

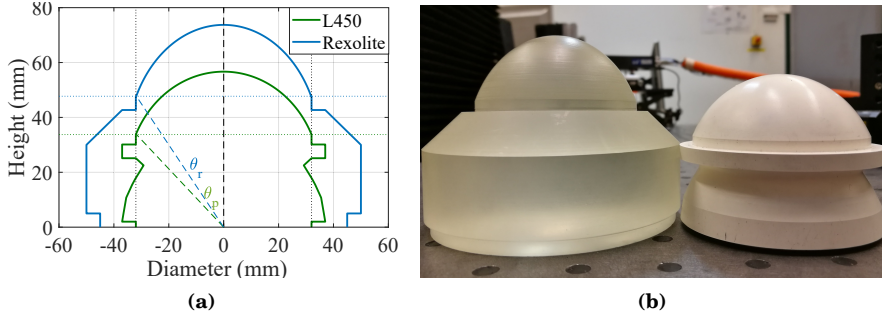


**Figure 3.6.** 2D-cut view of the designed ILAs, and (b) fabricated ILAs with L450 (right) and Rexolite (left) materials. Reprinted from [III].

The simulation and measurement results presented in Fig. 3.7 highlights that the boresight gain of the ILAs are comparable. At 73 GHz, the measured boresight gain of the Rexolite and L450 ILAs are 28.7 dBi and 29.4 dBi, respectively. While, the total loss between the two ILAs are equivalent, the major source of loss is different. In the case of the Rexolite ILA, the spillover loss, 2.74 dB, is maximum whereas, in the case of the L450 ILA, the dielectric loss of 3.7 dB is the most significant.

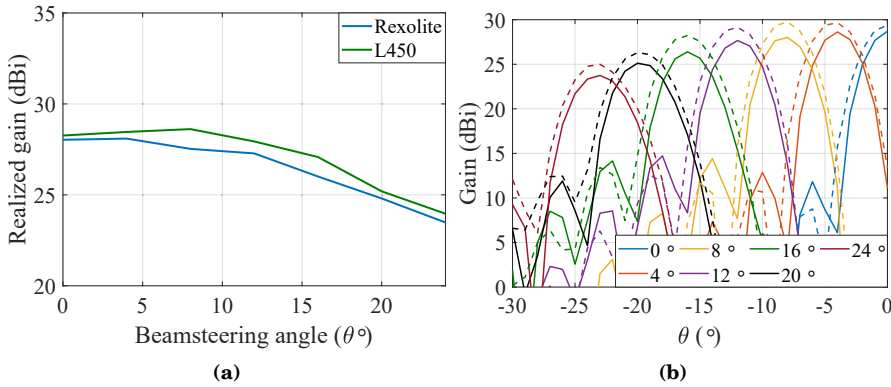


**Figure 3.7.** Measured (a) peak realized gain and (b) gain radiation pattern comparison of the Preperm-ILA (---) and Rexolite-ILA (—) at 73 GHz. Reprinted from [III].

The WR-10 OEWG feed is translated away from the focal center to steer the beams. The feed is moved at the step of 3.1 and 1.65 mm for the Rexolite and L450 ILAs respectively, to achieve  $-3$ dB beam-overlapping. To achieve the steering angle of  $24^\circ$ , the WR-10 feed is moved to an 18.6 and 9.9 mm offset position for Rexolite and L450 ILA, respectively. The smaller feed offset position for the L450-ILA is due to the smaller focal distance compared to the Rexolite-ILA. At a  $24^\circ$  steering angle, the scan loss of the Rexolite- and L450-ILAs are

4.9 dB and 4.3 dB, respectively. The lower scan loss of the L450 ILA is mainly due to the smaller feed offset position and the directive radiation pattern of the WR-10 OEWG due to the high  $\epsilon_r$  of L450 material.

The work demonstrates that the focal length and feed area of an ILA can be decreased by using high  $\epsilon_r$  material. The  $\tan\delta$  of the high  $\epsilon_r$  material might be the limiting factor when designing high gain ILA. Compared to a traditional ILA, the scan loss can be minimized by shaping the collimating surface. However, the scan loss of 4.5 dB and steering range of  $24^\circ$  must be improved to make it commercially viable.

### 3.4 Dual-spherical integrated lens antenna

The extension of the beamsteering range and reduction of the scan loss by placing the feeds along the focal arc is demonstrated in [III]. An extended hemispherical lens antenna is designed with the Teflon ( $\epsilon_r = 2.1$  and  $\tan\delta = 0.001$ ) material and its  $f/d$  is 1.22. The diameter and focal length of the Teflon lens are 52 mm and 63.5 mm, respectively (see Fig. 3.8). Sixteen Vivaldi feeding antennas are positioned on the spherical surface of radius 37.5 mm to steer the main beam to  $\pm 40^\circ$ . The  $1 \times 16$  beam-switching network is implemented with an SP4T RF switches. The lens and beam-switching feed array are designed to operate at the lower E-band, that is, 71-76 GHz.

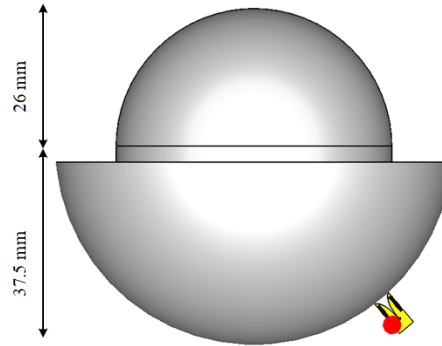


**Figure 3.8.** Extended hemispherical ILA with a Vivaldi feed on the spherical surface. Reprinted from [III].

The comparison between the simulated and measured peak realized gain is shown in Fig. 3.9 (a). The measured realized gain of all the beams peak at the designed frequency range. The peak measured realized gain of 19.6 dBi with the beam-switching network is attained by beam 7 at 71 GHz. Within the frequency range of interest, the difference between the simulated and measured gain of beam 7 varies between 0.8 to 3.4 dB. The radiation leakage from the end-launch connector could be the source of additional loss. The normalized radiation pattern comparison between the measurement and simulation is shown in Fig. 3.9 (b). For the  $\pm 40^\circ$  steering angle, the simulated directivity



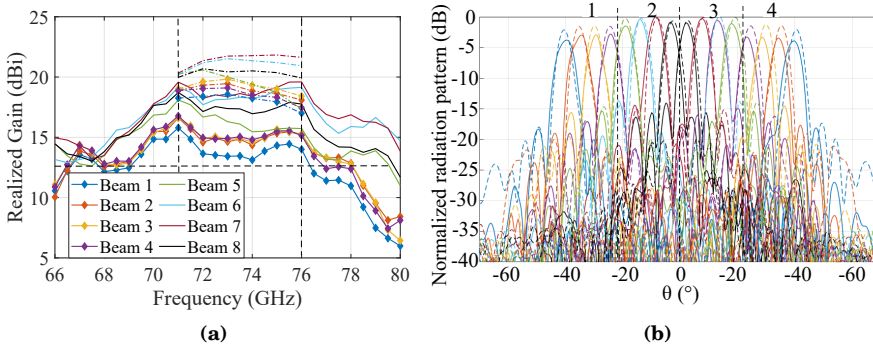


**Figure 3.9.** Comparison between simulated (---) and measured (—) (a) peak realized gain, and (b) normalized radiation pattern at 71 GHz of the dual-spherical ILA. Reprinted from [III].

scan loss of the dual-spherical ILA is 0 dB or negligible. With the realistic beam-switching feed network, the simulated gain scan loss of beam 1 is 1.5 dB compared to beam 8. The scan loss is caused by the longer transmission line length of the feed elements at larger offset positions. The measured scan loss of the dual-spherical ILA with the feeding network is 2.8 dB with respect to beam 8. The measured scan loss of the dual-spherical ILA for  $\pm 40^\circ$  steering angle excluding the beam-switching network loss with the feed 1 and 16 are 1.2 and 1.3 dB, respectively. The higher measured scan loss is potentially due to the radiation blockage and reflections from the metallic support structure that is used during measuring.

The dual-spherical ILA in [III], constant- $\epsilon_r$  spherical lens in [108] and Luneburg lens in [92] have feed antennas on a curved surface. The ILA design in [III] steers the main beam to  $\pm 40^\circ$  whereas, both the constant- $\epsilon_r$  spherical [108] and Luneburg lens in [92], managed to achieve the ultra-wide scanning range of  $\pm 90^\circ$ . The operation of dual-spherical ILA [III] is like constant- $\epsilon_r$  spherical lens [108], therefore, the scanning range of the ILA can be improved with careful choice of feed location and material permittivity. The  $f/d$  ratio of the lenses in [III], [108], and [92] are 1.2, 1.4, and 1, respectively. In case of the constant- $\epsilon_r$  spherical lens, the feeds are not in direct contact with the lens which leads to higher  $f/d$  as compared to the traditional hemispherical ILA in [III]. The  $f/d$  ratio of the Luneburg lens is equal to 1, however the manufacturing of the Luneburg lens is challenging, especially a 3D Luneburg lens. The simulated efficiency of the dual-spherical lens presented in [III] is approx. 50% which is comparable to the constant- $\epsilon_r$  spherical lens, whereas the efficiency of the flat Luneburg lens is 66%. All the lens antennas, [III], [108], and [92], steers the main beam along one plane and positioning of the feeds to steer the main beam in both planes is challenging with the curved feeding surface.

### 3.5 Integrated metal-plate lens

The operation of a lens antenna can be explained based on the electrical path length equality of the rays propagating through various segment of collimating surface. Compared to the free space, the length of the electrical path is shorter when the wave is passing through a medium that has  $\epsilon_r < 1$  and longer when  $\epsilon_r > 1$ . The electrical path length of a traditional ILA can be shortened by replacing the freespace, with material that has  $\epsilon_r < 1$ . Materials with  $\epsilon_r < 1$  does not exist in nature. However, an effective  $\epsilon_r$  between 0 and 1 can be realized when the wave is propagating through parallel plates. An off-body metal-lens antenna based on the parallel plates along the E-plane was proposed in [109] and later applied in various applications [110]–[112]. In [IV], an integrated metal-plate lens (IMLA) is designed by combining the traditional dielectric lens and the metal-plate lens to shorten the focal length as shown in Fig. 3.10.

Based on the ray path equality principle, the interface between the dielectric lens and the metal plate lens can be calculated as:

$$(\epsilon_r - \epsilon_{rm})y^2 + 2\sqrt{\epsilon_r}f(\sqrt{\epsilon_r} - \sqrt{\epsilon_{rm}})y + \epsilon_r z^2 = 0 \quad (3.1)$$

where  $\epsilon_{rm} = 1 - \left(\frac{\lambda_0}{2a}\right)^2$  is the effective relative permittivity of the metal-plate lens and  $a$  is the parallel plates separation distance. Since the effective relative permittivity  $\epsilon_{rm}$  is dependent on frequency, the operating bandwidth of the IMLA is limited.

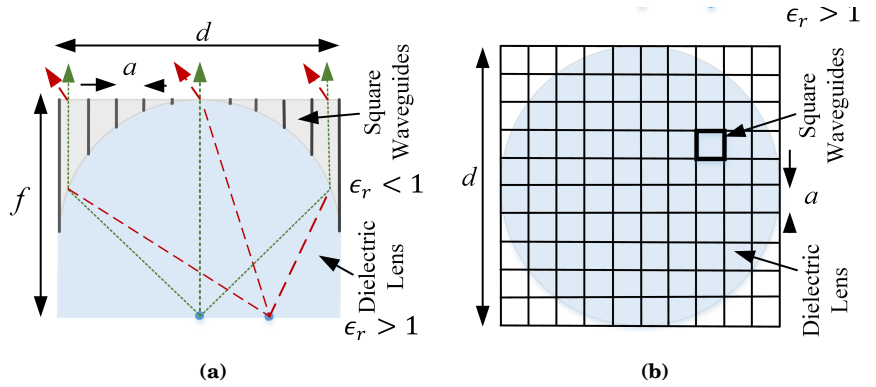


**Figure 3.10.** (a) Side view and (b) top view of the integrated metal-lens antenna (IMLA). Reprinted from [IV].

#### 3.5.1 Volumetric analysis

In [IV], the variation in the focal length,  $f$ , of an IMLA with varying  $\epsilon_r$  of the dielectric lens and  $\epsilon_{rm}$  of the metal-plate lens is studied with full-wave simulations. The effective relative permittivity of the metal-plate lens can be varied by changing the separation distance,  $a$ , between the plates. Fig. 3.11

(a) shows that the  $\epsilon_{rm}$  between 0 to 0.95 can be achieved by varying  $a$  between  $(0.5-2)\lambda_0$ .

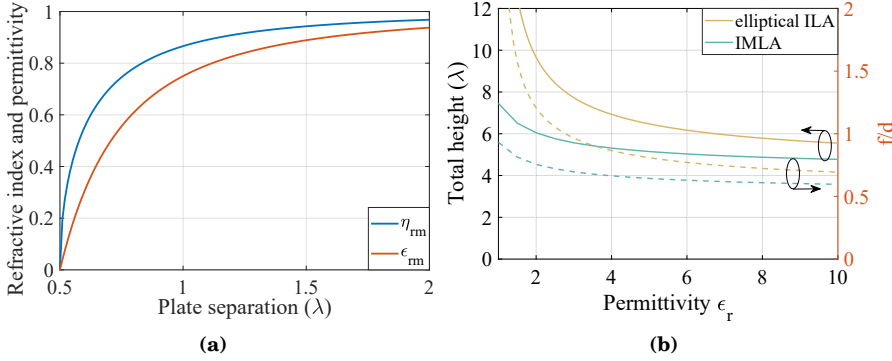


**Figure 3.11.** Relation between the parallel plates separation  $a$  and effective permittivity  $\epsilon_{rm}$  and refractive index  $\eta_m$  of the medium. Total height and  $f/d$  ratio comparison between the elliptical ILA and the IMLA for varying material permittivity. Radius is  $4\lambda_0$  and  $a = 0.6\lambda_0$ .

As a traditional ILA, the focal length or height of the IMLA decreases with increasing  $\epsilon_r$ . Fig. 3.11 (b) shows that the  $f/d$  ratio of an IMLA is shorter than that of the traditional ILA with the dielectric material of same  $\epsilon_r$ . The reduction of the  $f$  of an IMLA is more effective with low  $\epsilon_r$  materials, for example, with  $a = 0.6\lambda_0$ , for low  $\epsilon_r$  material such as Teflon, the  $f$  decreases by approx. 36%, whereas for materials with  $\epsilon_r = 10$ , the  $f$  decreases by 14%.

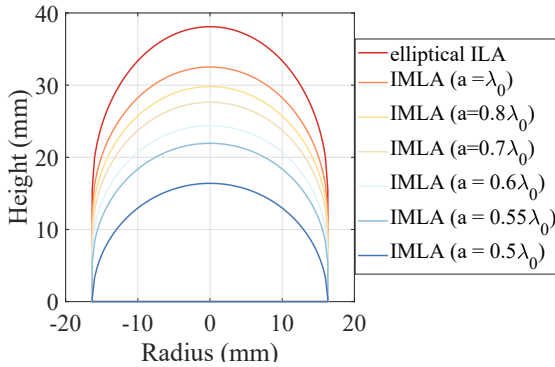


**Figure 3.12.** Collimating surface profile of the dielectric lens and the height comparison between elliptical ILA and the I-MLA with varying plate separation. Radius of the lens is  $4\lambda_0$  at 73.5 GHz. Metal-lens is not shown. Reprinted from [IV].

The change in the IMLA height and the shape of the dielectric-metal interface with respect to plate separation distance,  $a$ , is shown in Fig. 3.12. The  $f$  of an IMLA can be decreased with a smaller  $a$ . The eccentricity of the dielectric-metal interface also decreases with reduced  $a$ . When  $a = \infty$ , i.e. no metal-plate lens, the eccentricity and shape of the lens same as the elliptical ILA, i.e.  $e = 1/\sqrt{\epsilon_r}$ , and when  $a = 0.5\lambda_0$ , the shape of the dielectric-metal boundary is hemispherical,

i.e.  $e = 0$ .

Peak directivity comparison of the  $4\lambda_0$  IMLA designed with Teflon dielectric material illustrates that with the decreasing  $\epsilon_{rm}$  the directivity and directivity bandwidth of the IMLA decreases (see Fig. 3.13 [a]). The dielectric gradient at the dielectric-metal interface increases with decreasing  $a$ . The increasing impedance mismatch creates higher reflection towards the back direction as shown in Fig. 3.13 (b). Therefore, the matching layer between the dielectric and metal-plate lens is essential for the optimal performance of the IMLA.

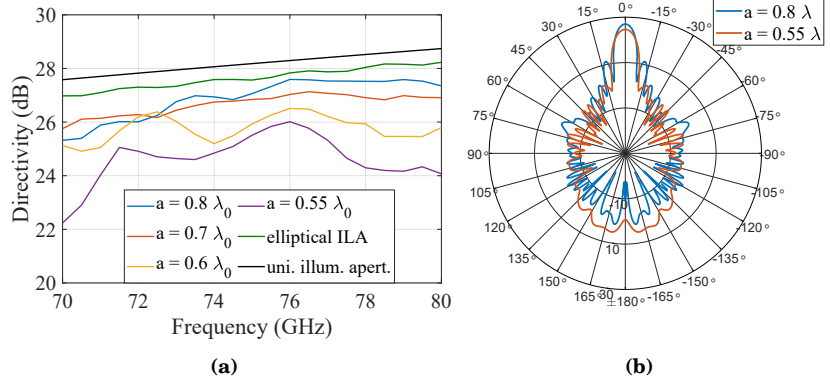


**Figure 3.13.** (a) Peak boresight directivity and (b) directivity radiation pattern w.r.t. varying plate separation  $a$  of  $4\lambda_0$  IMLAs with Teflon material. In (a), the black line represents the directivity of uniformly illuminated aperture of same dimensions. Reprinted from [IV].

In [IV], an IMLA is designed and simulated with Teflon material and metal-plate lens with  $a = 0.575\lambda_0$  to operate at 73.5 GHz, as shown in Fig. 3.14. The design shows that the height of the IMLA is 35% smaller than the traditional elliptical ILA designed with Teflon material. The simulation results also demonstrate that the gain and efficiency of the IMLA are comparable with the traditional elliptical ILA at the designed frequency. The simulated 3-dB gain bandwidth of the IMLA is 9% between 71 and 78 GHz (see Fig. 3.15 [a]). Fig. 3.15 (b) shows that the simulated scan loss of the IMLA, 7.4 dB for a 30° steering angle, is comparable to a traditional ILA.

The feasibility of combining the metal-plate lens and dielectric lens to shorten the focal length of a traditional ILA is studied. The volumetric analysis of the IMLA with the simulations show that the IMLA provides a significant reduction in the focal length while maintaining efficiency. However, the reduction in bandwidth, substantial scan loss, and fabrication complexity are the primary drawbacks. It is important to note that a small  $f/d$  can be achieved with an IMLA without using lossy or rare high  $\epsilon_r$  materials as discussed in [II]. The  $f/d$  of the IMLA designed in [IV] is comparable to that of an elliptical ILA designed with silicon,  $\epsilon_r = 11.7$ .

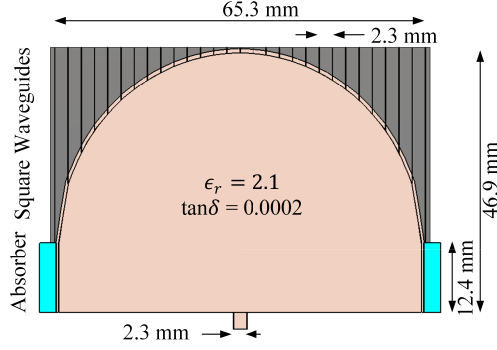


**Figure 3.14.** Cut view of the designed  $8\lambda_0$  I-MLA structure with matching layer.

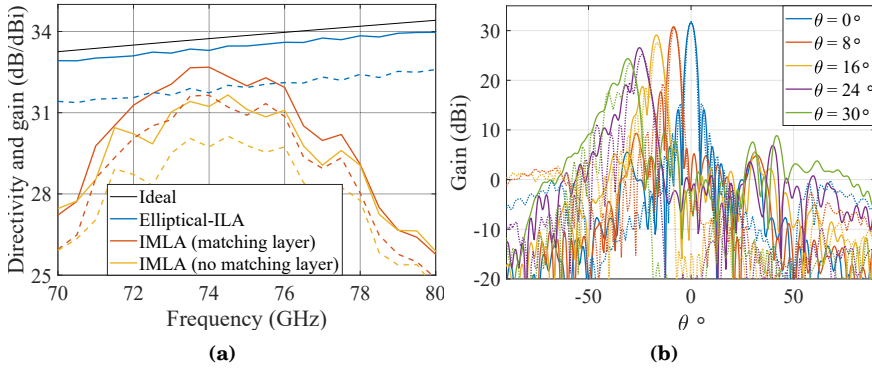


**Figure 3.15.** Maximum gain (- -) and directivity (—) comparison of elliptical ILA and IMLA with matching layer and without matching layer w.r.t. frequency. Lens radius is  $8\lambda_0$  at 73.5 GHz. Gain radiation pattern comparison between I-MLA (—) with matching layer and elliptical ILA (· ·) w.r.t. various beam steering angles. Lens radius is  $8\lambda_0$  at 73.5 GHz. Reprinted from [IV].

### 3.5.2 Fabrication

The practical implementation and performance improvement of the IMLA are further studied in [V]. An IMLA of  $16\lambda_0$  diameter is designed to operate at the center frequency of 73.5 GHz. The dielectric lens is constructed by machining the HDPE material. The simulation model of the designed IMLA with the matching layers and square-waveguide feed is shown in Fig. 3.16.

The metal-plate lens is manufactured by assembling 58 laser-cut stainless steel plates, that means, 29 plates in each orthogonal directions. The separation between the plates is  $0.56\lambda_0$ . The intersecting slots are made in the plates to interleave the plates in orthogonal directions (see Fig. 3.17). Initially, the thickness of the plates and intersecting slot width was equal to  $50\ \mu\text{m}$ . The focal length of the IMLA is  $11.1\lambda_0$  and the  $f/d$  is equal to 0.69. The square waveguide with a 3.09 mm radiating aperture width is used as a feed antenna. The impact of the feed directivity on the IMLA performance is similar to the traditional ILAs. Since, the  $f/d$  and extension length of the IMLA are smaller than the

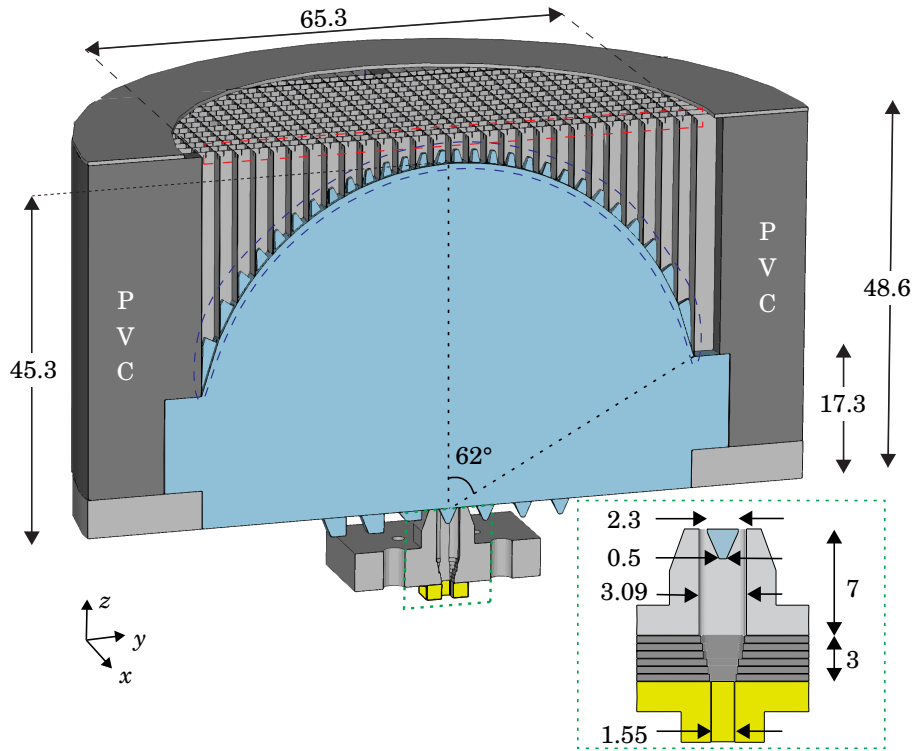


**Figure 3.16.** Orthographic view with the E-plane cut of the IMLA showing the dielectric-metal (blue dashed line) and waveguide-air (red dashed line) matching layers. The inset shows the  $yz$  cross-section view of the square waveguide (light grey), waveguide-lens dielectric pin (blue), the transition plates (dark grey), and WR-12 waveguide (yellow). Dimensions are in mm. Taken from [V].

traditional ILA, the optimum feed directivity is lower. The optimum gain of the  $16\lambda_0$  IMLA and traditional ILA with HDPE material is achieved with 12-dB and 14-dB feed directivity, respectively.

Two matching layers are implemented at the dielectric-metal interface and the metal-air interface to minimize the reflections as shown in Fig. 3.16. The matching layer at the dielectric-metal interface is designed by corrugating the right trapezoidal dielectric pins on the surface of the dielectric lens. The matching layer between the metal-plate lens and the free space is implemented by cutting the trapezoidal slots in the metal plates, as shown in Fig. 3.17. Both matching layers are designed to minimize the reflections upto  $30^\circ$  steering angle of the IMLA. The matching layers improve the simulated gain of the IMLA by 1.4 dB. With both the matching layers, the  $f/d$  increases to 0.74.

The full-wave simulation of the IMLA shows that the IMLA operates at the designed frequency. At 74 GHz, the simulated peak directivity and gain are 32.5 dB and 31.8 dBi, respectively. The aperture and radiation efficiencies are greater than 50% and 83 % between 71-76 GHz. The simulated peak total efficiency is 64%.

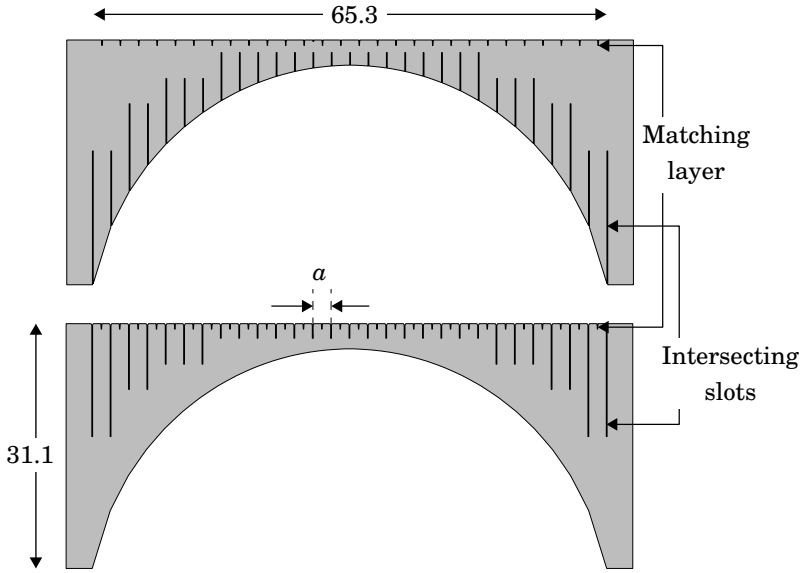


**Figure 3.17.** 2D CAD drawing of the center plates placed along the orthogonal direction/planes of the metal-plate lens. Dimensions are in mm. Taken from [V].

To ease the fabrication, the thickness of the stainless steel plates and the intersecting slot widths are revised to  $80\text{ }\mu\text{m}$  and  $105\text{ }\mu\text{m}$ , respectively. The changes in dimension of the metal-plate lens shift the IMLA operation towards a higher frequency. The fabricated dielectric lens, metal-plate lens and the assembled IMLA are shown in Fig. 3.18 (a), (b) , and (c), respectively.

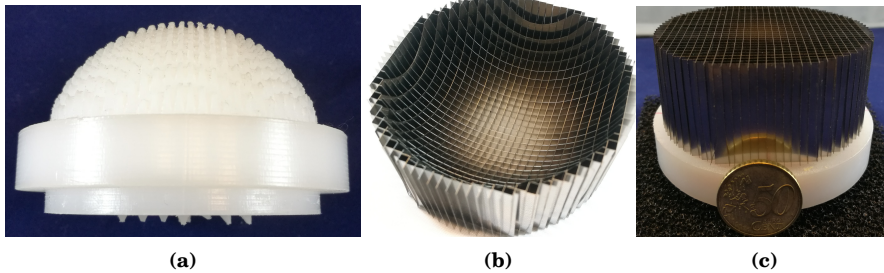


**Figure 3.18.** (a) The dielectric lens, (b) the metal-plate lens, and (c) the combination of the metal-plate lens (top) and dielectric lens (bottom) to form the IMLA. Taken from [V].

The back-propagated amplitude and phase distribution at the radiating aperture illustrate that the IMLA operates as designed (see Fig. 3.19). When the square waveguide feed is at the focal center, the phase distribution is mostly flat across the radiating aperture. At 76 GHz, the simulated and measured peak realized gain towards the boresight direction is 31.2 dBi and 31 dBi, respectively.

Good agreement between the simulation and measurement results confirms

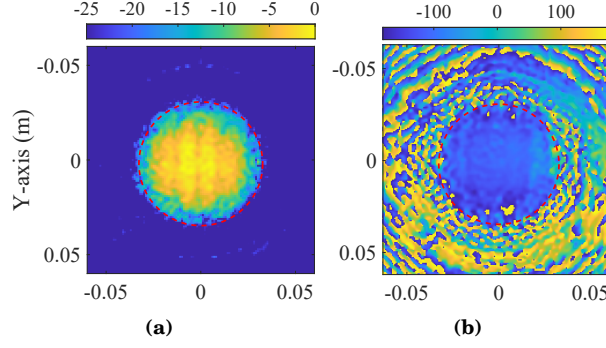


**Figure 3.19.** Electric-field (a) amplitude and (b) phase (right) pattern at the aperture of the IMLA while radiating towards boresight. Taken from [V].

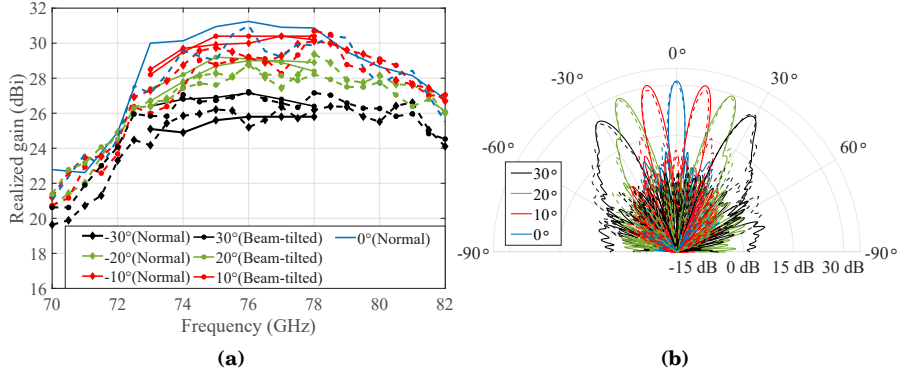


**Figure 3.20.** Comparison between the simulated (—) and measured (- -) radiation pattern of IMLA with beam-tilt: right and without beam-tilt: left, along the (a) H-plane and (b) E-plane at 76 GHz. Taken from [V].

the possibility of IMLA fabrication. In future designs, the clearance and tolerance required to assemble the metal-plate lens should be considered during the design phase to achieve a better match between the simulation and fabrication model. In comparison to  $f/d$  1.1 of a traditional ILA presented in [I], the IMLA limits the  $f/d$  to 0.69 or 0.74 with matching layers. The total efficiency of the IMLA, 64%, is superior to the traditional ILA, 45% [I].

### 3.5.3 Scan-loss reduction

The IMLA presented in [V] is designed to steer the main beam to  $\pm 10^\circ$ ,  $\pm 20^\circ$ , and  $\pm 30^\circ$ . The main beam is steered by placing the square waveguide feed to  $\pm 5$  mm,  $\pm 10$  mm, and  $\pm 15$  mm from the focal center. The work in [V] also aims to minimize the scan loss at higher steering angles.

The enhancement of scanning properties is realized by tilting the radiation pattern of the focal plane feeds at the offset positions. The radiation pattern tilting is achieved by introducing an asymmetric dielectric pin at the radiating aperture of the square waveguide, as shown in Fig. 3.21. The asymmetric



and symmetric dielectric pins are machined in the IMLA focal plane as shown in Fig. 3.18. The beam-tilting direction is determined by the amount of the refracted and refracted-and-reflected fields on the waveguide radiating aperture as shown in Fig. 3.21. Due to the difference in amplitude distribution along the E- and H-plane of the TE<sub>10</sub> mode propagating in the square waveguide, the beam-tilting direction is different between them.

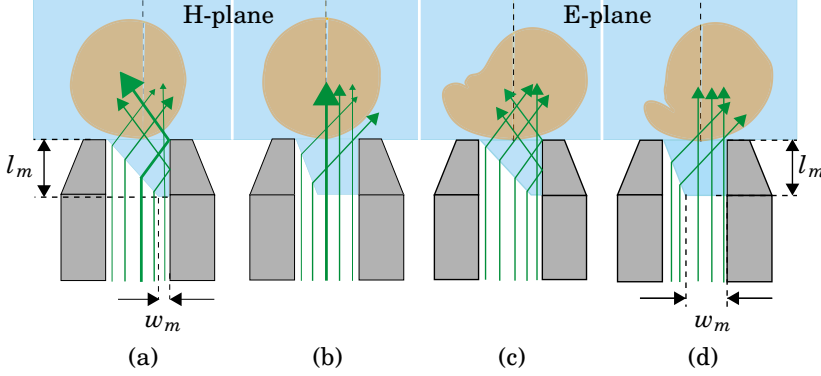


**Figure 3.21.** Simplified ray illustration (green) of the beam tilting and radiation patterns (yellow) at 73.5 GHz. (a) and (b) shows the operation along the H-plane for the pins designed to tilt the beam 12° and 15° in H- and E-planes, respectively. (c) and (d) shows the operation along the E-plane for the same pins, respectively. Note, that the waveguide radiates to the same dielectric material as the pin is made of. Taken from [V].

The beam-tilting angle of the square waveguide is controlled by changing the shape of the dielectric pin, that is, by varying the length  $l_m$  and bottom width  $w_m$  of the dielectric pin. The radiation pattern of the square waveguide feed with varying  $l_m$  and  $w_m$  for E- and H-planes are shown in Fig. 3.22 and 3.23, respectively. The maximum main lobe inclination of 12° and 15° is achieved along the H- and E-plane, respectively.

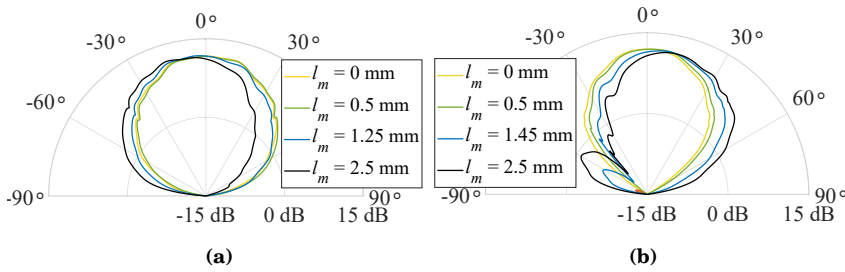


**Figure 3.22.** Beam tilting of the square waveguide along (a) H-plane when  $w_m = 0.5$  mm and (b) E-plane when  $w_m = 2$  mm w.r.t. length  $l_m$  of the asymmetric dielectric pin at 73.5 GHz. Taken from [V].

The asymmetric dielectric pins are positioned along the positive X- and Y-axis at the offset position of 5 mm, 10 mm and 15 mm along both E- and H-plane (see Fig. 3.24). The symmetric dielectric pins are positioned at the same offset distance along the negative X- and Y-axis. The symmetric dielectric

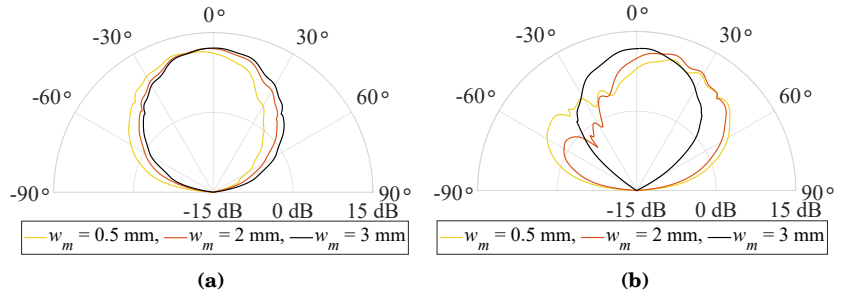


**Figure 3.23.** Beam tilting of the square waveguide along (a) H-plane and (b) E-plane w.r.t. bottom width  $w_m$  when  $l_m = 2.5$  mm of the asymmetric dielectric pin at 73.5 GHz. Taken from [V].

pins are designed to minimize the feed reflection coefficient without affecting the radiation pattern.

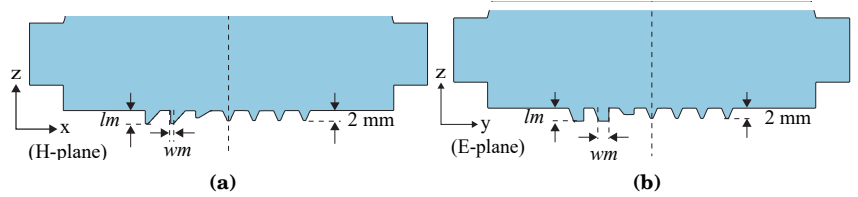


**Figure 3.24.** Symmetric pins: reference feeds along positive X and Y-axis, and asymmetric pins: beam-tilting feeds along negative X- and Y-axis, arrangement along the focal plane of the IMLA for the (a) H-plane and (b) E-plane beam steering. Taken from [V].

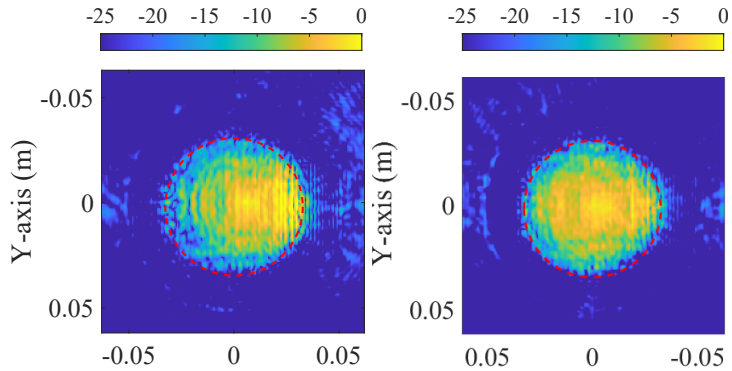


**Figure 3.25.** Electric-field amplitude at the aperture of the IMLA when beam is steered to (a)  $-30^\circ$  (without beam-tilt) and (b)  $30^\circ$  (with beam-tilt) along the H-plane. Figure (b) is rotated  $180^\circ$  to ease comparison with (a). Taken from [V].

The IMLA aperture amplitude distribution improves due to the feed inclination as shown in Fig. 3.25. The asymmetric dielectric pin boosts the IMLA gain in both the simulation model and fabricated prototype, as shown in Fig. 3.26 and 3.20, respectively. The results show that the gain improvement is higher for larger steering angles. For a  $30^\circ$  steering angle along the H-plane, the measured

scan loss is 3.8 and 5.8 dB with and without the feed beam-tilting at 76 GHz. The measurement results show, at  $30^\circ$  along the H-plane, that the improvement in the IMLA gain is more than 1 dB for the frequency range between 73 and 78 GHz. The radiation pattern comparison shows that the tilting of the feed beam improves the first SLL.

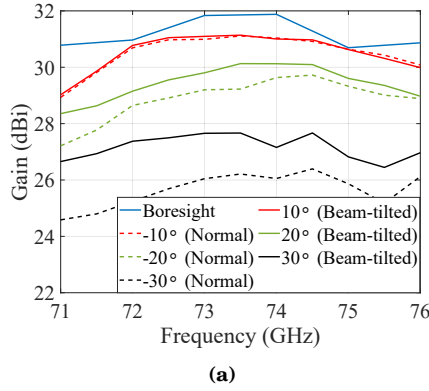


**Figure 3.26.** Comparison of the simulated peak gain of the IMLA with (—) and without ( - -) feed-beam tilting in the H-plane. Taken from [V].

It is important to note that, the scan loss of an IMLA is minimized without compromising the boresight gain as in many other techniques [60], [75], [85]. In addition, the feed antennas are positioned along the focal plane rather than the focal arch, which makes the design of the feed array for 2D beamsteering considerably easier.

## 4. Beam-switching network

### 4.1 Introduction

A beam-switching antenna has an array of input ports or radiating elements, and the excitation of each port generates the main beam in different directions. Generally, one input port is excited at a given time. The selection of the desired input port from an array of ports is done by the network of RF-switches, in other words, a beam-switching network.

During the simulation studies or prototyping and characterizing an ILA, a single feed element is used and the same feed is moved across the focal plane or arc to steer the beam. However, in practice, an array of elements are present at a close proximity, and these array elements interact and affect each others' performance. In other words, there is mutual coupling between the closely placed array elements. As discussed in section 2.3.3, the beam cross-over criteria, the smaller  $f/d$  of the ILA, and dimensions of the radiating element lead to smaller separation between the beam-switching array elements. In general, the smaller separation between the array elements result in higher coupling. The mutual coupling with inactive/switched-OFF elements might change the radiating and impedance properties of the active/switched-ON feed element, thereby affecting the performance of the ILA. In [VI], the effects on the ILA performance due to mutual coupling and impedance mismatch between the feed array elements are studied.

High insertion loss and passive beam steering drawbacks of the BSA with the RF-switch-based BSN are discussed in Section 2.2.2. The RF-switch provides a high ON-OFF ratio, approx. 25 dB, which ensures the leakage from unwanted ports has a minimal effect on the radiation pattern. Similarly, the ON-OFF ratio or isolation between the active and inactive ports of BSA can be achieved with the beamforming chips used in PAA. The literature study shows that the beamforming chips can provide upto 30 dB amplitude and 360° phase control [30], [35]. A high ON-OFF ratio can be achieved with beamforming chip by assigning maximum gain to the desired input port and a minimum gain to OFF ports.

The feasibility, challenges and advantages of implementing the BSN with a beam-former chips are studied in [VII].

#### 4.2 Effect of feed mutual coupling on ILA

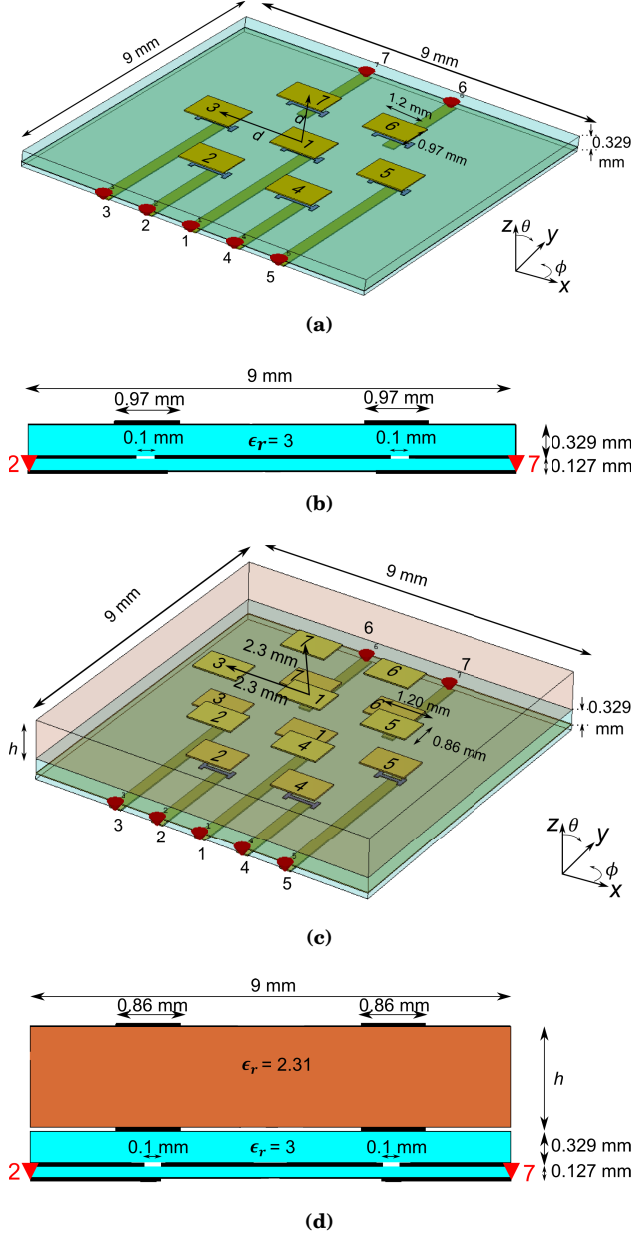


**Figure 4.1.** Orthographic and yz-plane cross section views at  $x = -1.15$  mm for the embedded ACMPA (EA) (a) and (b), and embedded stacked ACMPA (ESA) (c) and (d), respectively. Reprinted [VI].

In this work, the effects of the mutual coupling between the feed array elements on the ILA performance are studied. The far-field properties of the elliptical ILA of 160-mm diameter, presented in [I], are investigated with the following two types of feed antennas: 1) aperture coupled microstrip patch antenna (ACMPA) and 2) stacked ACMPA. Both feed antennas are embedded with the identical radiating elements around them, as shown in Fig. 4.1. The far-field radiation patterns of center element, denoted by 1 in Fig. 4.1, of both the feed array antenna are simulated with CST Microwave studio. The simulated far-field radiation patterns are used as the source in the ray-tracing simulations of 160-mm ILA. Then, the ILA directivity, radiation pattern, and beamsteering properties are studied with ray-tracing simulations.

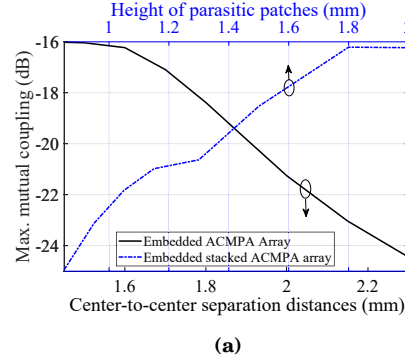


**Figure 4.2.** Maximum mutual coupling,  $|S_{j1}|$ , levels of the EA and ESA feeds with the varying  $d$  and  $h$ . Reprinted [VI].

The separation between the array elements,  $d$ , and the distance of the parasitic patch,  $h$ , of the embedded ACMPA (EA) and embedded stacked ACMPA (ESA) feeds are varied to change the mutual coupling between the center and the surrounding radiating elements. The coupling between the array elements is evaluated based on the transmission coefficient,  $|S_{j1}|$ , where  $j = 2 - 9$ , between the feed ports of the array elements. Fig. 4.2 shows that, when the  $d$  is varied between 1.5 and 2.3 mm for EA feed and  $h$  is varied between 2 mm to 0.85 mm, the change in maximum  $|S_{j1}|$ , is similar, that is, between -16 dB to -25 dB.

The radiation patterns of the EA and ESA feeds respond differently to the change in  $d$  and  $h$ , though the couplings,  $|S_{j1}|$ , are at a similar level as shown in Fig. 4.3 (a) and (b). In the case of the EA feed, a null appears in the radiation pattern towards the boresight direction when  $d < 1.6$  mm. The distortion in the ESA radiation pattern is lower compared to EA feed. The radiating aperture amplitude and phase pattern of the 160-mm ILA, shown in Fig. 4.3 (c) and (d), corresponds well with their feed radiation patterns. The aperture amplitude and phase pattern of the 160-mm ILA with EA feed show greater distortion as compared to the ESA feed. The peak far-field directivity of the 160-mm ILA fed with the EA decreases by approx. 5 dB when the  $|S_{j1}|$  between the feeds changes from -25 dB to -16 dB. For similar variation in the coupling levels,  $|S_{j1}|$ , of the ESA feed, the change in the peak directivity of the 160-mm ILA is below 0.5 dB.

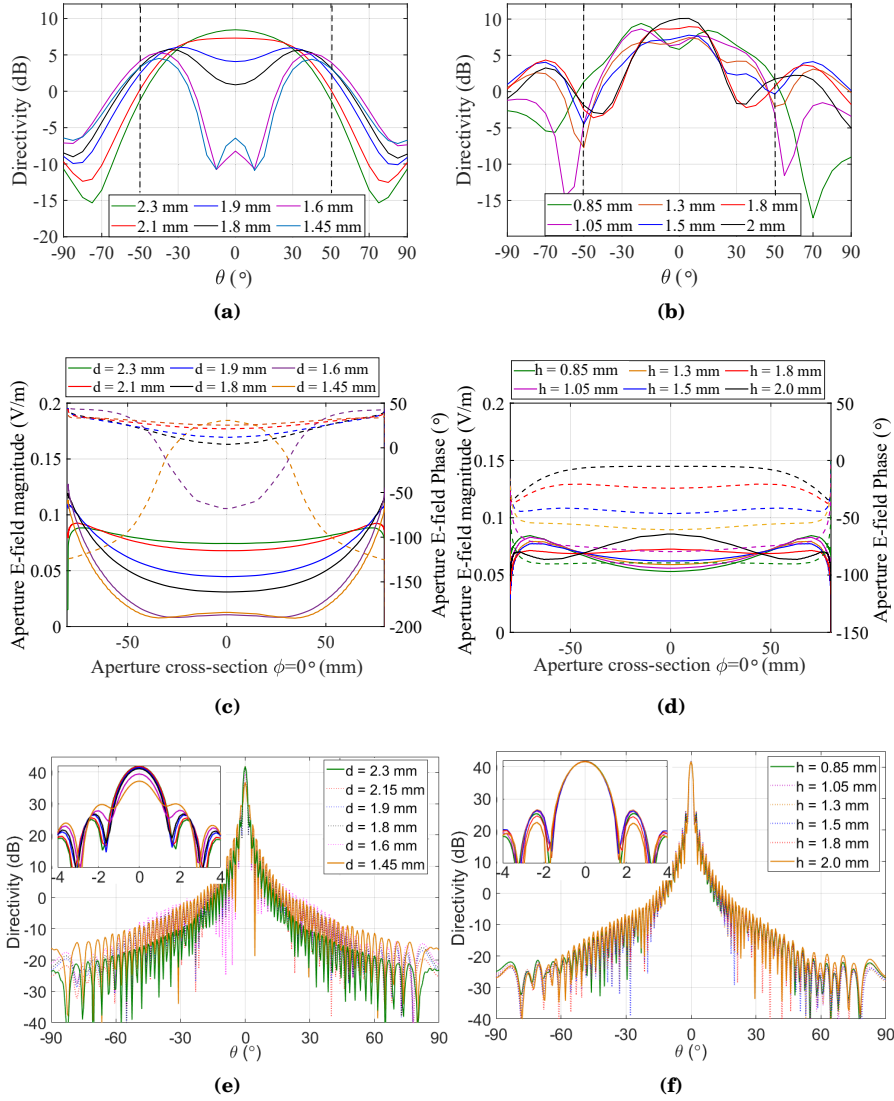


**Figure 4.3.** Directivity radiation pattern of the (a) EA and (b) ESA feed, amplitude and phase distribution at the aperture surface of the ILA with (c) EA and (d) ESA array feed, and ILA directivity pattern with the (e) EA and (f) ESA feed in the  $\phi = 0^\circ$  (H-plane) cut with varying mutual coupling level i.e. with varying element separation  $d$  and parasitic patch distance  $h$ , respectively. Reprinted [VI].

The study of the 160-mm ILA far-field properties with the EA and ESA feeds, which have similar mutual coupling,  $|S_{j1}|$ , levels but different active element radiation patterns, helped to conclude that the  $|S_{j1}|$ , alone is not a reliable metric to estimate the effects on ILA. However, the possible distortion of the embedded feed radiation pattern has significant effects on the ILA radiation pattern. From the feed antenna design perspective, to precisely estimate the ILA performance, evaluation of the embedded feed's radiation pattern is more

essential than the  $|S_{j1}|$ .

The impedance of the active or switch-ON port of the RF switch might be close to the characteristics impedance. However, the impedance of the surrounding inactive or switch-OFF ports can be arbitrary. The effects of the impedance mismatch between the active and the surrounding inactive elements are studied with simulations. As the EA radiation pattern shows minimal variation with respect to change in the inactive port impedances, the study is conducted with only the ESA feed. The center element is considered as the active element whose impedance is assigned to be  $50\Omega$ . The port impedance of the remaining ports varies from 1 to  $2500\Omega$ . The impedance of the surrounding inactive ports was assigned in three different ways: 1) equal and real, 2) equal and complex, and 3) unequal and real.

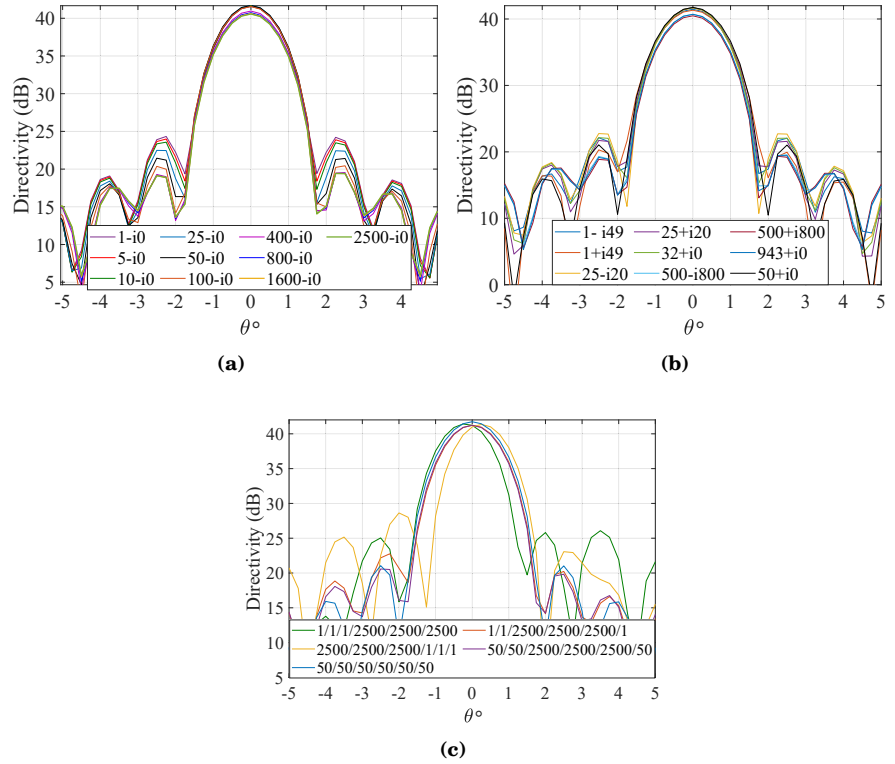


**Figure 4.4.** Radiation pattern variation of the ILA w.r.t. (a) equal and real, (b) equal and complex and (c) unequal and real port impedances variation of the surrounding switched-OFF elements. Reprinted [VI].

The simulation study shows that the change in port impedance of the surrounding inactive elements has negligible effect on the reflection coefficient  $|S_{11}|$  of the active port, whereas the coupling between the active and inactive ports,  $|S_{j1}|$ , decreases. The effect on the ILA performance is proportional to the changes/distortion in the feed radiation pattern. When the surrounding inactive port impedances are equal and varied from 1 to  $2500\Omega$ , the 160-mm ILA peak



directivity and SLL change by 1 dB and 5 dB, respectively, as shown in Fig. 4.4 (a) and (b). Fig. 4.4 (c) illustrates that the systematic assignment of unequal port impedance to the surrounding inactive feed can change the beam steering direction of the ILA.

### 4.3 Beam-reconfigurable antenna with Rotman lens

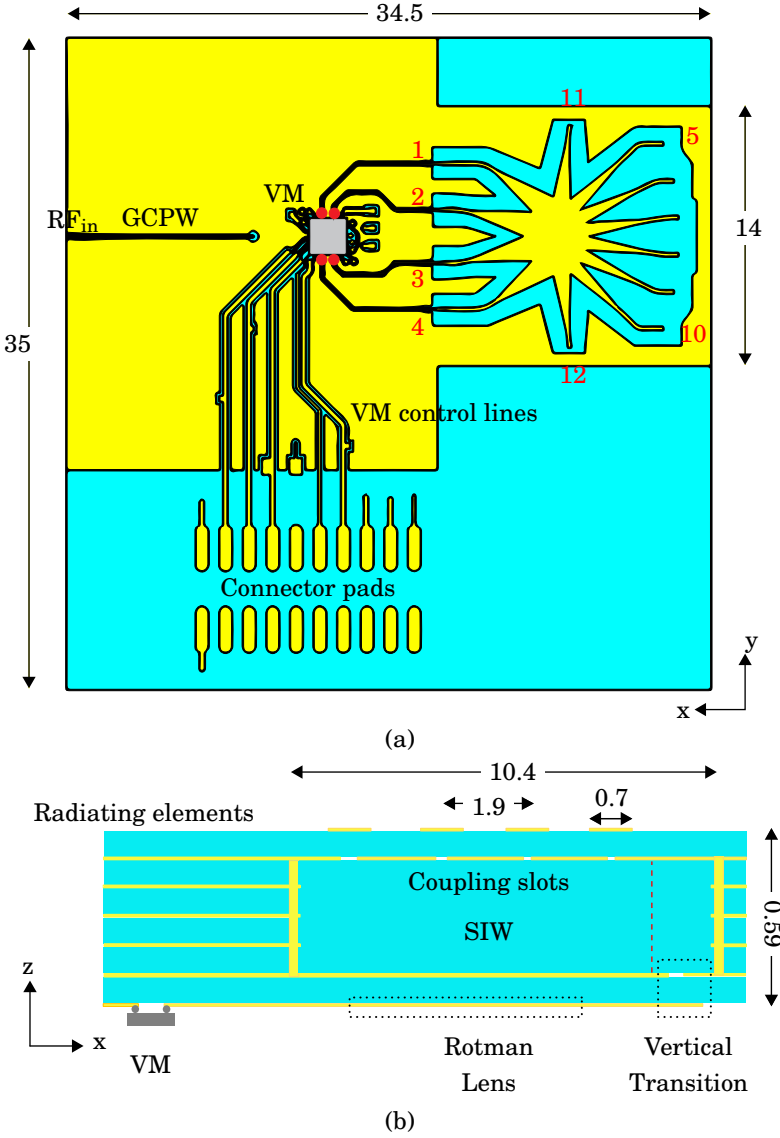


**Figure 4.5.** (a) Bottom view and (b) cross-section of the Rotman lens-based beam-switching array on LTCC detailing the location of VM, Rotman lens, vertical transition, SIW and microstrip patch array. Dimensions are in mm. Reprinted from [VII].

The BSA with the Rotman lens and the substrate-integrated waveguide (SIW) fed microstrip patch antenna array is presented in [VII]. The antenna is designed on the 6-tape-layer Low Temperature Co-fired Ceramics (LTCC) substrate with  $\epsilon_r = 5.7$  and  $\tan\delta = 0.002$ . The thick-film gold material of  $5\text{-}\mu\text{m}$  thickness and  $\sigma = 7 \times 10^6 \text{ S/m}$  conductivity is used as the conductor.

The Rotman lens has four beam ports, (1-4), that is positioned to steer the main beam to  $-30^\circ$ ,  $-10^\circ$ ,  $10^\circ$  and  $30^\circ$ , as shown in Fig. 4.5 (a). The Rotman lens has six array ports, (5-10), which are connected to six  $1 \times 4$  SIW-fed series arrays via the vertical transition as shown in Fig. 4.5 (b). The separation between the array ports is 2 mm along the  $y$ -axis. The Rotman lens has two dummy ports (11-12).

#### 4.3.1 SIW-fed $1 \times 4$ series array

The SIW-fed microstrip patch antenna arrays are used as radiating elements in [VII]. Four radiating microstrip patch antennas are placed along the broad wall of SIW. The RF power is coupled to the antenna through the transverse slots in the ground plane. The excitation amplitude and phase of the series array elements need to be equal. The excitation amplitude of the patch antenna is dependent on the width of the coupling slot, the position of the slot and the current density of the SIW [113].

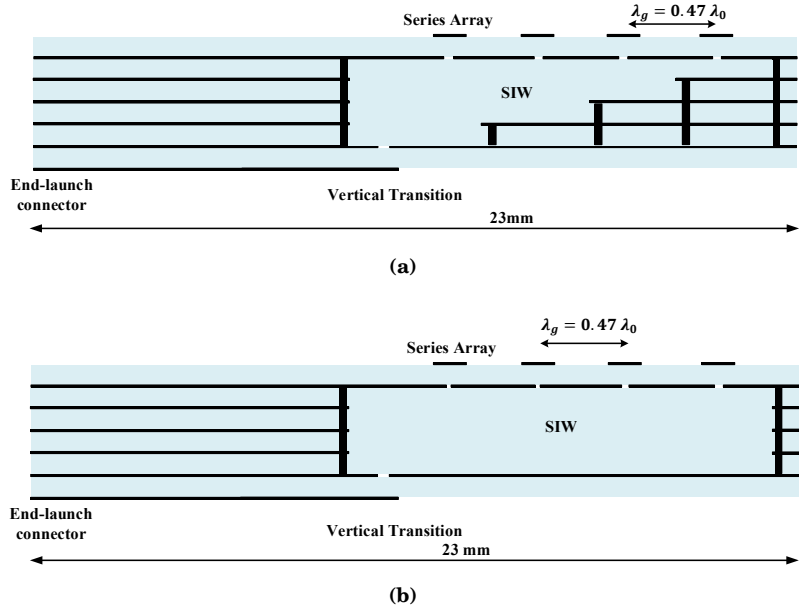


**Figure 4.6.** Schematics of (a) the stepped-SIW fed and (b) the uniform-SIW fed  $1 \times 4$  array with the end-launch connector. Reprinted from [VIII].

In [VIII], two SIW-fed  $1 \times 4$  microstrip antenna arrays are designed based on different admittance control mechanisms. The excitation amplitude of the array elements is controlled in the following ways: 1) varying the height of the SIW

used in a stepped-SIW fed array, and 2) varying the coupling slot width used in a uniform-SIW fed array. The schematic diagrams of the series arrays are shown in Fig. 4.6 and the dimensions are detailed in [VIII]. For both series arrays, the separation between the array elements is 1.9 mm,  $(0.47\lambda_0)$  and the dimensions of the radiating patch are the same  $(0.7 \times 1.05 \text{ mm}^2)$ .

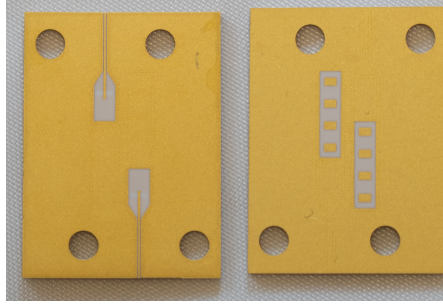


**Figure 4.7.** Top and bottom view of the stepped-SIW and uniform-SIW fed  $1 \times 4$  series arrays on LTCC substrate. Reprinted from [VIII].

The fabricated prototypes are shown in Fig. 4.7. The far-field radiation pattern and gain are measured with the planar near-field measurement. The simulated peak directivity of both series arrays is greater than 10 dB between 71-76 GHz. The measured peak gain of both series array is approx. 8 dBi. The main lobe of both the series arrays are towards the boresight direction and the radiation pattern is symmetrical about the axis, thereby illustrating that equal power is coupled to each microstrip patch antenna (see Fig. 4.8 [a]). Similarly, the numerically back-propagated aperture field illustrates that the series array elements are radiating with almost equal power and phase as shown in Fig. 4.8 (b).

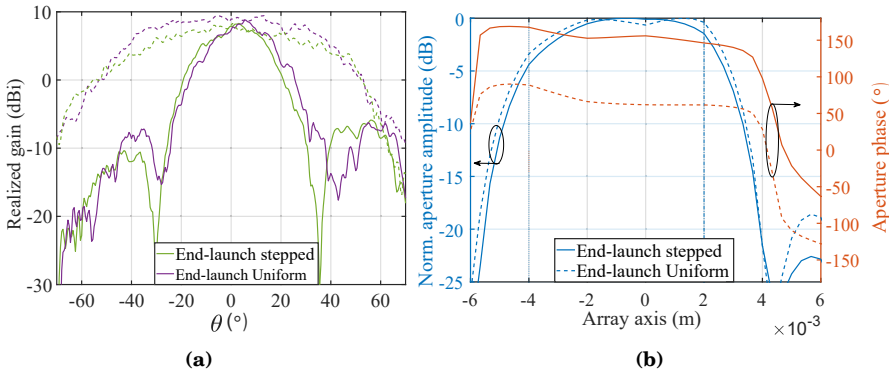


**Figure 4.8.** (a) The measured E-plane (—) and H-plane (---) realized gain radiation pattern, and (b) the aperture amplitude and phase along array axis of the end-launch connector fed arrays at 75 GHz. Reprinted from [VIII].

While, the performances of both series arrays are similar, based on ease in manufacturing, the stepped-SIW fed array can be a better choice as the

stepped-SIW fed array does not have stringent tolerance on the width of the slots. Since, the design of the Rotman lens-based BSA was finalized before the study of admittance control techniques, the uniform-SIW fed  $1 \times 4$  microstrip patch antenna arrays are used as the radiating element in [VII].

#### 4.3.2 Vertical transition

To make the BSA compact, the radiating elements, that is, six  $1 \times 4$  series arrays, and the microstrip Rotman lens are positioned on top of each other on different LTCC layers. The RF signal from the microstrip line (MSL) of the Rotman lens array ports is coupled to the SIW by the vertical transitions. The vertical transition is implemented with the  $0.4 \times 1.8 \text{ mm}^2$  coupling slot on the common ground plane between the MSL and the SIW. The vertical transition is designed to operate at 71-76 GHz.

Fig. 4.9 (a) presents bottom view of the fabricated and measured back-to-back vertical transition. The simulated and measured S-parameter results show that the vertical transition operates over a wide frequency band 70-80 GHz (see Fig. 4.9(b)). The measured insertion loss of a single transition is 1.2 dB. The transmission line losses and the radiation from the microstrip stub are major sources of the insertion loss.

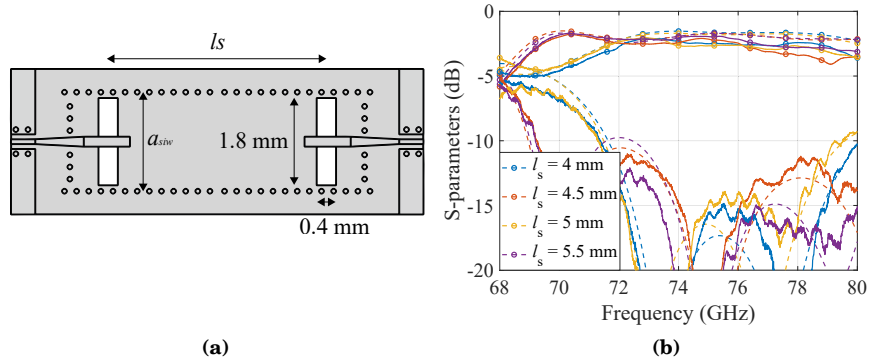


**Figure 4.9.** (a) Bottom view, and (b) the simulated (---) and measured (—) S-parameter i.e.  $|S_{11}|$  (—) and  $|S_{12}|$  (---), comparison of the back-to-back vertical transition structures with different lengths,  $l_s$ . Reprinted from [VIII].

#### 4.3.3 Vector modulator IC as RF switch

In this work, the BSN is implemented using a 4-channel vector modulator (VM) instead of the traditional RF switches. The VM allows to independently control the excitation amplitude and phase of each beam port of the Rotman lens. A single channel of the vector modulator provides the maximum gain of 24 dB,  $|S_{21}|$ , at 75 GHz. The vector modulator provides  $360^\circ$  phase control upto 17 dB gain.

The top and bottom views of the fabricated Rotman lens-based beam-reconfigurable antenna are shown in Fig. 4.10. The VM is attached to the LTCC module using the flip-chip connection. The LTCC module is fed with the 1-mm end-launch connector. The length of the grounded coplanar waveguide (GCPW) and stripline transmission lines from the end-launch connector to the input of the vector modulator are 10 mm and 4.1 mm, respectively. The simulated transmission line loss between the end-launch connector feed and VM ranges between 8-11 dB between 71-76 GHz frequency range. At 75 GHz, the simulated total efficiency of beam port 1 and 2 from the output of VM are 6.4 dB and 5.8 dB, respectively. The losses of the beam port 1 is slightly higher due to longer transmission line length and increase in the spillover loss coupling into the dummy ports.

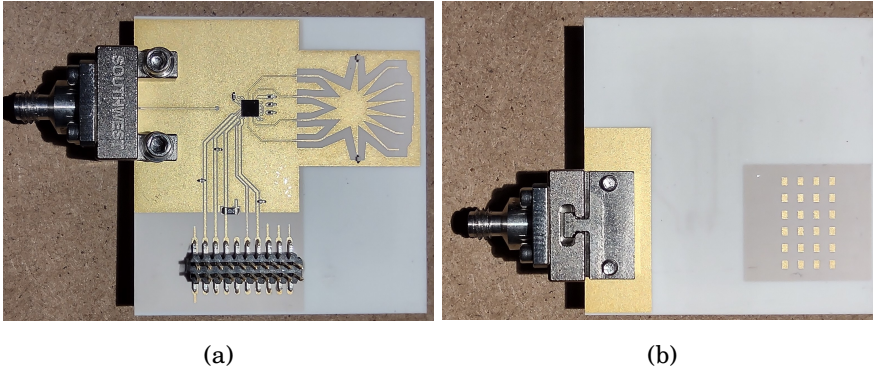


**Figure 4.10.** (a) Bottom view and (b) top view of the fabricated prototype of the Rotman lens-based beam-switching array on LTCC assembled with the end-launch connector. Reprinted from [VII].

In contrast to an RF switch, all the output ports of the specific VM are in switch-ON mode. A single channel of a VM can independently provide numerous states of amplitude control by increasing the gain. The VM is used as the switching element by increasing the gain of the desired channel while maintaining the remaining ports at minimum gain states.

Fig. 4.11 (a) illustrates the situation when all beam ports are excited with equal amplitude the radiation pattern is wide. With the increasing gain of the single input port, the radiation pattern becomes directive and steers the main beam towards the intended direction of the excited beam port. The simulation studies show that the approx. 21 dB higher excitation amplitude of the switch-ON port with respect to OFF port result in the peak directivity and SLL difference below 0.1 dB and 1 dB, respectively, compared to the ideal beam-switching scenario. The measured radiation pattern of beam port 2 with a maximum VM gain of 24 dB also shows good agreement with the ideal beam-switching scenario. The good agreement between the simulated and measured normalized radiation pattern of all four beam ports demonstrates that a VM can be used for beam-switching element (see Fig. 4.11 (b).)

The simulated beam port 2 directivity and realized gain of the BSA without

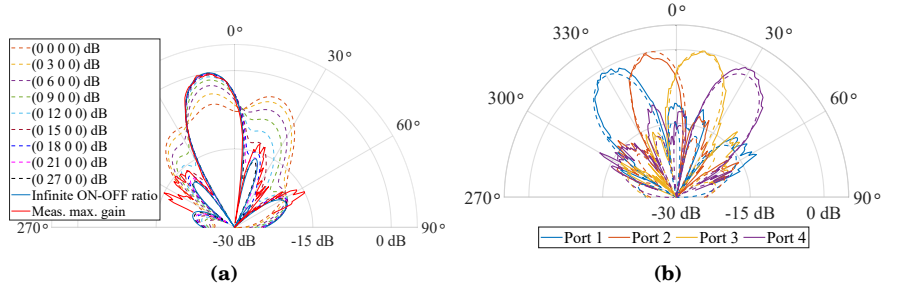


**Figure 4.11.** Simulated (---) and measured (—) normalized radiation pattern comparison (a) of beam port 2, where the simulation excitation amplitude is increased from 0-27 dB, (b) four beam ports. Reprinted from [VII].

the VM are 17.5 dB and 11.5 dBi, respectively. The measured gain of the LTCC module, with maximum VM gain, is 20 dBi. The measured gain of the LTCC module is approx. 14 - 15 dB lower than the expected, 35 dBi. The RF leakage and impedance mismatch at the flip-chip connection are potential sources of losses. It is important to note that, the measured gain with the BSN is greater than the simulated realized gain without the BSN (see Fig. 4.12). In contrast, to traditional BSN, the VM-based BSN provides gain, instead of insertion loss, which increases the radiated power.

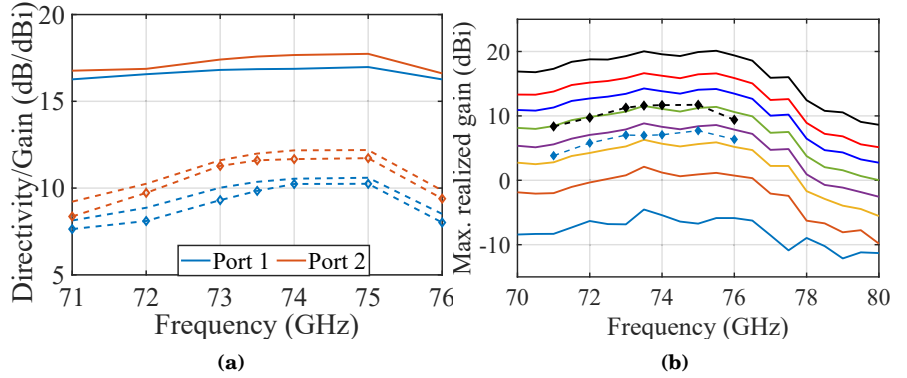


**Figure 4.12.** (a) Simulated directivity (—), gain (---), and realized gain (---) comparison and (b) simulated (---) and measured (—) realized gain comparison of the Rotman lens-based beam-switching array on LTCC. Simulated results do not include VM gain. Reprinted from [VII].

#### 4.3.4 Beam-reconfigurability

The VM also allows simultaneous excitation of multiple beam ports with desired amplitude and phase. The simultaneous excitation of the multiple beam port facilitates beam reconfigurability. When multiple beam ports are simultaneously excited, the resulting radiation pattern is the vector sum of the combined beam-port radiation patterns. The simultaneously excited beam ports and

their excitation amplitudes and phases are determined by the desired radiation pattern.

Fig. 4.13 (a) illustrates that two beam ports can be simultaneously excited to generate various types of radiation pattern: a multi-beam, a flat-top, or a directive beams. The simultaneous excitation of the adjacent beam ports is particularly interesting as it helps to improve the cross-over levels of the combining beams. The cross-over level of the beam ports 1&2, 2&3, and 3&4 are  $-3$  dB,  $-5.4$  dB and  $-3.7$  dB, respectively. The main lobe of the simultaneously excited beam ports 1&2, 2&3, and 3&4 are directed towards  $-19^\circ$ ,  $0^\circ$  and  $19^\circ$ , respectively, and the peak gains are approx. 6 dB higher than the beam cross-over level.

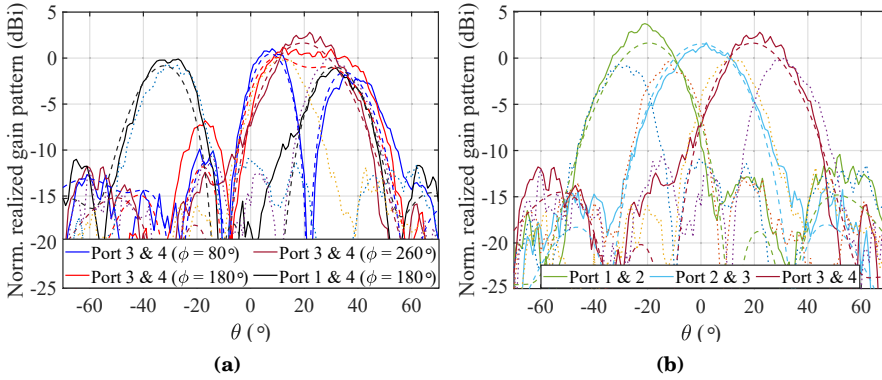


**Figure 4.13.** Simulated (---) and measured (—) normalized radiation pattern comparison when two beam ports are simultaneously excited to demonstrate (a) various two-port combinations and (b) improved beam cross-over level with the adjacent two beam ports excitation. The measured pattern (···) of combining beam port 1, 2, 3, and 4 are also plotted for reference. Reprinted from [VII].

The wider radiation pattern can be achieved by increasing the number of simultaneously excited beam ports. In Fig. 4.14 (a) and (b), three and four adjacent beam ports are excited with equal amplitude and the phases are optimized to generate wide beams. The simulated HPBW of the resulting far-field radiation pattern with simultaneous three and four beam port excitation are  $51^\circ$  and  $75^\circ$ , respectively. The directivity decreases and the HPBW increases with the increasing number of simultaneously excited beam ports. However, with the simultaneous excitation of 2, 3, and 4 ports the RF power increases by 3 dB, 4.77 dB, and 6 dB, respectively. Therefore, the EIRP of the directive beam and the simultaneously excited wider beams are similar.

The work demonstrates that the VM-based BSN can generate both directive and wide beams, and improve the beam cross-over level. In this work, the HPBW ranges from  $18^\circ$  to  $75^\circ$ . However, the possible reconfiguration depends on the original design of passive BFN. There are two potential drawbacks of the VM based beam-switching network. First, the VMs cannot operate with full potential in the beam-switching network since all the VM channels are not

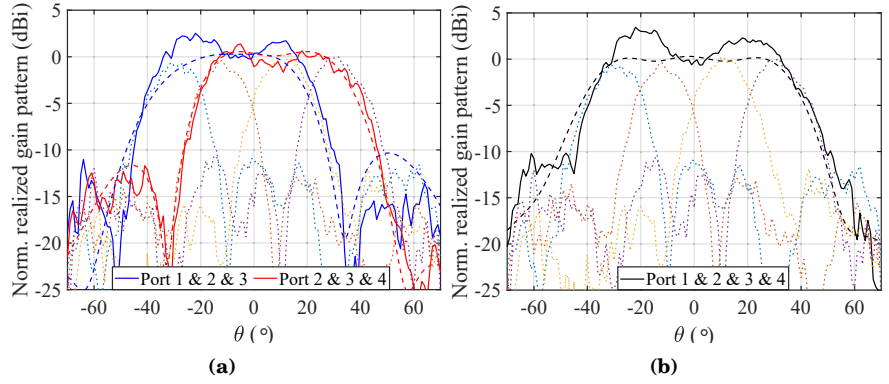


**Figure 4.14.** Comparison between the simulated (---) and measured (—) normalized radiation patterns, when (a) three, and (b) four adjacent beam ports are simultaneously excited with the appropriate phase. The individually measured beams (···) are plotted for reference. Reprinted from [VII].

excited to maximum gain. Second, the RF leakage from the undesired ports reduce the ON-OFF ratio and consequently distort the radiation pattern.

The VM based beam-switching feed network can be used to feed an ILA which helps to achieve the beam-reconfigurability and improve the beam cross-over level.





## 5. Summary of publications

### **Publication I: Lens Antenna Design for E-band Point-to-point Radio Links**

This work presents the simulation and measurement results of the 160-mm elliptical integrated lens antenna. The ILA is designed to operate at E-band (i.e. 71–76/81–86 GHz) and complies with the ETSI regulations for point-to-point link antennas. The paper also discusses the optimum relative permittivity and feed directivity to maximize the ILA gain. An aperture coupled stacked microstrip patch antenna was studied with simulations to improve the boresight gain and scan loss of the ILA.

### **Publication II: Integrated Lens Antennas for E-Band**

In this work, the effect of the dielectric properties, relative permittivity, and loss tangent on the ILA performance is studied. Two ILAs are designed using Rexolite ( $\epsilon_r = 2.53$  and  $\tan\delta = 0.0013$ ) and PREPERM L450® ( $\epsilon_r = 5.01$  and  $\tan\delta = 0.0046$ ) materials. The efficiency, boresight gain, and scan loss up to  $24^\circ$  steering angles of the two elliptical ILAs are compared with simulations and measurements. The work also presents the results of the free space relative permittivity characterization of the L450 material at millimeter-wave frequencies.

### **Publication III: Beam-Switching Dual-Spherical Lens Antenna with Low Scan Loss at 71–76 GHz**

An extended hemispherical ILA with feeds on the spherical surface is designed and characterized to minimize the scan loss upto  $\pm 40^\circ$  steering angle. The dual-spherical ILA is fabricated of Teflon ( $\epsilon_r = 2.1$  and  $\tan\delta = 0.001$ ) and the radius of the radiating aperture is 26 mm. A conformal  $1 \times 16$  linear beam-switching feed array based on SP4T switches and Vivaldi antennas is designed to feed the ILA. The Vivaldi feed elements are positioned along the spherical surface of radius 37.5 mm. The dual-spherical lens and the feed array are designed to operate at the lower E-band (71–76 GHz). The maximum simulated and measured realized

gain including the switch network losses are 21.8 and 19.6 dBi, respectively. The measured gain scan loss of the ILA excluding the switch network loss is less than 1.3 dB in the lower E-band for beams within  $\pm 40^\circ$ .

#### **Publication IV: Integrated Metal-lens Antennas with Reduced Height at 71–76 GHz**

A low-profile lens based on the combination of metal-plate lens and dielectric lens, namely integrated metal-plate lens (IMLA), is introduced. The volumetric analysis of the IMLA based on the relative permittivity and parallel plate separation distance is studied. The paper also presents full-wave simulation results of an IMLA of  $16\lambda_0$  diameter designed with Teflon ( $\epsilon_r = 2.1$  and  $\tan\delta = 0.0002$ ) and parallel plate at the separation distance of  $0.575\lambda_0$  to operate at 73.5 GHz.

#### **Publication V: Low-profile Scanloss-Reduced Integrated Metal-Lens Antenna**

An IMLA of  $16\lambda_0$  diameter is designed, fabricated, and characterized in this work. The IMLA is designed with the HDPE ( $\epsilon_r = 2.31$ ,  $\tan\delta = 0.0002$ ) and laser-cut parallel plates with the separation of  $0.56\lambda_0$  to operate at 73.5 GHz. The feed beam-tilting of the square waveguide feed is implemented to minimize the scan loss. The IMLA design can achieve a low profile ( $0.69 f/d$ ) and high radiation efficiency (92%). The gain bandwidth of the IMLA is 9.9 %. Moreover, the simulated and measured scan loss was reduced to 4.1 dB and 3.8 dB for a  $30^\circ$  steering angle with feeds on the focal plane.

#### **Publication VI: Effect of mutual coupling between feed elements on integrated lens antenna performance**

The effects of mutual coupling between the beam-switching array antennas on the ILA performance are studied in this work. The aperture coupled microstrip patch antenna (ACMPA) and stacked ACMPA feeds embedded in an array are used as feed. The radiation pattern of the EA and ESA feeds with varying mutual coupling,  $|S_{j1}|$ , are used to study the radiation characteristics of the ILA. It is found that the mutual coupling,  $|S_{j1}|$ , level alone does not predict the changes in the ILA radiation well. Results show that changes in the embedded radiation pattern of the feed have a significant impact on the ILA characteristics. Furthermore, the impact of the port impedance mismatch of the adjacent inactive antennas on the active element radiation pattern and its corresponding impact on the ILA are investigated.

#### **Publication VII: Beam-Reconfigurable Antenna Based on Vector Modulator and Rotman Lens on LTCC**

In this work, a  $4 \times 6$  Rotman lens is integrated with six  $1 \times 4$  series arrays on the LTCC substrate. The beam-switching antenna is designed to steer the main beam to  $\pm 10^\circ$ , and  $\pm 30^\circ$  at lower E-band. The beam-switching network is implemented with the 4-channel vector modulator integrated circuit. The measured peak gain with the VM is 20 dBi and the scan loss is less than 1 dB. The beam reconfigurability is demonstrated with the simultaneous excitation of the beam ports with optimum phase using the VM. The HPBW is varied from  $18^\circ$  to  $75^\circ$ .

#### **Publication VIII: Millimeter-Wave Stepped Series Array with LTCC**

In this work, two  $1 \times 4$  substrate integrated waveguide (SIW) coupled microstrip patch arrays are designed on the LTCC substrate. The admittance to the series array elements is controlled using the varying SIW height and varying coupling slot width. Both series arrays produce a symmetric radiation pattern towards the boresight direction and achieve the directivity greater than 10 dB between 71-76 GHz. Additionally, a MSL-SIW vertical transition structure is designed to facilitate the multi-layered RF structure in LTCC.



## 6. Conclusions

The research presented in this thesis focuses on the development and improvement of beam-switching antennas to meet the high-gain and beam-steering requirements of the new generation communication systems. The work can be divided into two aspects with regard to the beam-switching antennas: passive beamforming network, i.e. integrated lens antenna, and beam-switching networks. The research is mostly conducted at the lower E-band, i.e. 71-76 GHz. However, the results should be equally valid for other frequencies.

The research begins with the design and fabrication of the ILA with a 160-mm diameter, which meets the requirements for point-to-point radio link [I]. The 160-mm ILA also demonstrates that ILAs are bulky, have high loss, and significant scan loss. The research work in [II], [III], [IV], and [V] aims to make an ILA low-profile, efficient, and to minimize the scan loss.

The possibility and challenges of designing a low-profile ILA with high permittivity materials are studied in [II]. While, the high permittivity materials can reduce the ILA focal length, the high loss of high permittivity material could degrade or limit the achievable gain. The integrated metal-lens antenna (IMLA) enables the design low-profile lens from commonly available, low relative permittivity and low-loss materials. The concept, parametric study, and drawbacks of the IMLA are discussed in [IV]. In [V], the IMLA is fabricated with two matching layers at the dielectric-metal and metal-air interfaces to minimize the reflections. The simulation and measurement results confirm that the IMLA achieves high radiation efficiency and small form-factor. Ideally, the designed IMLA should support the dual-polarized operation, but the metal-plate lens assembly adds asymmetry and may have effect on the polarization performance, thus investigation with more simulations and measurements are needed in future.

The second aspect of the ILA that the research investigates in detail is the scan loss. In [II], the scan loss of the Rexolite-ILA and L450-ILA are minimized by designing elliptical collimating surfaces with the minor axis greater than radius. However, the improvement in the scan loss is limited in [II]. The positioning of the feed antennas along the spherical surface minimizes the scan loss of the extended hemispherical ILA to negligible, as demonstrated in [III].

Implementation of 2D beamsteering with the feeds on the curved surface is challenging. The scan loss reduction technique for the feeds positioned along the focal plane is demonstrated in [V]. The radiation pattern tilting of the feeds at the offset positions along the focal plane decreases the scan loss of the IMLA. The proposed solution does not require compromising the boresight performance to achieve low scan loss. The beam-tilting mechanism implemented in [V], operates differently for each polarization. The beam-tilting mechanism that supports the dual-polarized operation and other antenna types, such as microstrip patch antenna, should be developed.

The second part of the thesis studies the beam-switching network that feeds a BSA. The effects of mutual coupling and impedance mismatch between the closely placed beam-switching array elements on the ILA properties are studied in [VI]. The numerical study suggests that the radiation pattern of the beam-switching feed is essential in determining the ILA radiation characteristics. Furthermore, the distortion of feed radiation pattern affects the ILA radiation pattern the most. The BSN for the Rotman lens-based BSA is implemented with the vector modulator as the switching element. The BSN based on the VM as switching element minimizes the insertion loss, facilitates the beam-reconfigurability, and improves the beam-crossover level. In the future, the VM-based BSN could also be implemented for the ILA feed.

The deployment of high-gain antennas is going to increase significantly in the near future. The broader objectives are to design low-cost and low power consuming antenna solutions that meet the high-gain and wide-beam-steering requirements. The beam-switching antennas have the potential to meet the requirements. The author believes that the knowledge developed during this research will help improve the performance of beam-switching antennas to meet the objectives.

# References

- [1] “Cisco annual internet report (2018–2023),” Cisco Systems, White paper, 2020.
- [2] “Looking ahead to 5G,” Nokia Networks, White paper, 2014.
- [3] “5G: A technology vision,” Huawei Technologies, White paper, 2013.
- [4] “5G wireless access: An overview,” Ericsson, White paper, 2020.
- [5] F. Boccardi, R. W. Heath, A. Lozano, T. L. Marzetta, and P. Popovski, “Five disruptive technology directions for 5G,” *IEEE Communications Magazine*, vol. 52, no. 2, pp. 74–80, 2014.
- [6] W. Roh, J.-Y. Seol, J. Park, B. Lee, J. Lee, Y. Kim, J. Cho, K. Cheun, and F. Aryanfar, “Millimeter-wave beamforming as an enabling technology for 5G cellular communications: theoretical feasibility and prototype results,” *IEEE Communications Magazine*, vol. 52, no. 2, pp. 106–113, 2014.
- [7] “NR; user equipment (UE) radio transmission and reception; part 2: Range 2 standalone,” 3GPP, Technical specification (TS) 38.101-2, Apr. 2021. [Online]. Available: <https://portal.3gpp.org/desktopmodules/Specifications/SpecificationDetails.aspx?specificationId=3284>
- [8] C. Dehos, J. L. González, A. D. Domenico, D. Kténas, and L. Dussopt, “Millimeter-wave access and backhauling: the solution to the exponential data traffic increase in 5G mobile communications systems?” *IEEE Communications Magazine*, vol. 52, no. 9, pp. 88–95, September 2014.
- [9] Z. Pi, J. Choi, and R. Heath, “Millimeter-wave gigabit broadband evolution toward 5G: fixed access and backhaul,” *IEEE Communications Magazine*, vol. 54, no. 4, pp. 138–144, April 2016.
- [10] J. Hasch, E. Topak, R. Schnabel, T. Zwick, R. Weigel, and C. Waldschmidt, “Millimeter-wave technology for automotive radar sensors in the 77 GHz frequency band,” *IEEE Transactions on Microwave Theory and Techniques*, vol. 60, no. 3, pp. 845–860, 2012.
- [11] D. Sheen, D. McMakin, and T. Hall, “Three-dimensional millimeter-wave imaging for concealed weapon detection,” *IEEE Transactions on Microwave Theory and Techniques*, vol. 49, no. 9, pp. 1581–1592, 2001.
- [12] T. S. Rappaport, S. Sun, R. Mayzus, H. Zhao, Y. Azar, K. Wang, G. N. Wong, J. K. Schulz, M. Samimi, and F. Gutierrez, “Millimeter wave mobile communications for 5G cellular: It will work!” *IEEE Access*, vol. 1, pp. 335–349, 2013.
- [13] J. G. Andrews, S. Buzzi, W. Choi, S. V. Hanly, A. Lozano, A. C. K. Soong, and J. C. Zhang, “What will 5G be?” *IEEE Journal on Selected Areas in Communications*, vol. 32, no. 6, pp. 1065–1082, June 2014.



- [14] R. Valkonen, "Compact 28-GHz phased array antenna for 5G access," in *2018 IEEE/MTT-S International Microwave Symposium - IMS*, 2018, pp. 1334–1337.
- [15] X. Gu, D. Liu, C. Baks, O. Tageman, B. Sadhu, J. Hallin, L. Rexberg, and A. Valdes-Garcia, "A multilayer organic package with 64 dual-polarized antennas for 28 GHz 5G communication," in *2017 IEEE MTT-S International Microwave Symposium (IMS)*, 2017, pp. 1899–1901.
- [16] K. Kibaroglu, M. Sayginer, T. Phelps, and G. M. Rebeiz, "A 64-element 28-GHz phased-array transceiver with 52-dBm EIRP and 8–12-Gb/s 5G link at 300 meters without any calibration," *IEEE Transactions on Microwave Theory and Techniques*, vol. 66, no. 12, pp. 5796–5811, Dec 2018.
- [17] G. Gültepe, S. Zihir, T. Kanar, and G. M. Rebeiz, "A dual-polarized 1024-element Ku-band SATCOM transmit phased-array with  $\pm 70^\circ$  scan and 43.5 dBW EIRP," in *2020 IEEE/MTT-S International Microwave Symposium (IMS)*, 2020, pp. 837–840.
- [18] Y. Aslan, J. Puskely, J. H. J. Janssen, M. Geurts, A. Roederer, and A. Yarovoy, "Thermal-aware synthesis of 5G base station antenna arrays: An overview and a sparsity-based approach," *IEEE Access*, vol. 6, pp. 58 868–58 882, 2018.
- [19] T. Semiconductor, *70-90 GHz SP4T Switch Flip Chip*, TriQuint Semiconductor, Nov. 2009. [Online]. Available: <https://datasheetspdf.com/pdf-file/720912/TriQuintSemiconductor/TGS4306-FC/1>
- [20] C. A. Balanis, *Antenna theory: analysis and design*. John Wiley & Sons, 2015.
- [21] D. M. Pozar, *Microwave engineering*. John Wiley & Sons, 2011.
- [22] W. L. Stutzman and G. A. Thiele, *Antenna theory and design*. John Wiley & Sons, 2012.
- [23] A. Rudge and N. Adatia, "Offset-parabolic-reflector antennas: A review," *Proceedings of the IEEE*, vol. 66, no. 12, pp. 1592–1618, 1978.
- [24] Y. Rahmat-Samii and A. C. Densmore, "Technology trends and challenges of antennas for satellite communication systems," *IEEE Transactions on Antennas and Propagation*, vol. 63, no. 4, pp. 1191–1204, 2015.
- [25] A. Artemenko, A. Mozharovskiy, A. Maltsev, R. Maslennikov, A. Sevastyanov, and V. Ssorin, "Experimental characterization of E-band two-dimensional electronically beam-steerable integrated lens antennas," *IEEE Antennas and Wireless Propagation Letters*, vol. 12, pp. 1188–1191, 2013.
- [26] A. Tamminen, S. Mäkelä, J. Ala-Laurinaho, J. Häkli, P. Koivisto, P. Rantakari, J. Säily, A. Luukanen, and A. V. Räisänen, "Reflectarray design for 120-GHz radar application: Measurement results," *IEEE Transactions on Antennas and Propagation*, vol. 61, no. 10, pp. 5036–5047, 2013.
- [27] A. Clemente, L. Dussopt, R. Sauleau, P. Potier, and P. Pouliguen, "Wideband 400-element electronically reconfigurable transmitarray in X band," *IEEE Transactions on Antennas and Propagation*, vol. 61, no. 10, pp. 5017–5027, 2013.
- [28] Q. Chen, O. Zetterstrom, E. Pucci, A. Palomares-Caballero, P. Padilla, and O. Quevedo-Teruel, "Glide-symmetric holey leaky-wave antenna with low dispersion for 60 GHz point-to-point communications," *IEEE Transactions on Antennas and Propagation*, vol. 68, no. 3, pp. 1925–1936, 2020.
- [29] R. J. Mailloux, *Phased array antenna handbook*. Artech House, 2017.

- [30] A. Nafe, M. Sayginer, K. Kibaroglu, and G. M. Rebeiz, “ $2 \times 64$ -element dual-polarized dual-beam single-aperture 28-GHz phased array with  $2 \times 30$  Gb/s links for 5G polarization MIMO,” *IEEE Transactions on Microwave Theory and Techniques*, vol. 68, no. 9, pp. 3872–3884, 2020.
- [31] X. Gu, D. Liu, C. Baks, O. Tageman, B. Sadhu, J. Hallin, L. Rexberg, P. Parida, Y. Kwark, and A. Valdes-Garcia, “Development, implementation, and characterization of a 64-element dual-polarized phased-array antenna module for 28-GHz high-speed data communications,” *IEEE Transactions on Microwave Theory and Techniques*, vol. 67, no. 7, pp. 2975–2984, 2019.
- [32] S. Shahramian, M. J. Holyoak, and Y. Baeyens, “A 16-element W-band phased-array transceiver chipset with flip-chip PCB integrated antennas for multi-gigabit wireless data links,” *IEEE Transactions on Microwave Theory and Techniques*, vol. 66, no. 7, pp. 3389–3402, 2018.
- [33] J. Pang, Z. Li, R. Kubozoe, X. Luo, R. Wu, Y. Wang, D. You, A. A. Fadila, R. Saengchan, T. Nakamura, J. Alvin, D. Matsumoto, A. T. Narayanan, B. Liu, J. Qiu, H. Liu, Z. Sun, H. Huang, K. K. Tokgoz, K. Motoi, N. Oshima, S. Hori, K. Kunihiro, T. Kaneko, A. Shirane, and K. Okada, “21.1 a 28 GHz CMOS phased-array beamformer utilizing neutralized bi-directional technique supporting dual-polarized MIMO for 5G NR,” in *2019 IEEE International Solid- State Circuits Conference - (ISSCC)*, 2019, pp. 344–346.
- [34] B. Sadhu, Y. Tousi, J. Hallin, S. Sahl, S. K. Reynolds, r. Renström, K. Sjögren, O. Haapalahti, N. Mazor, B. Bokinge, G. Weibull, H. Bengtsson, A. Carlinger, E. Westesson, J.-E. Thillberg, L. Rexberg, M. Yeck, X. Gu, M. Ferriss, D. Liu, D. Friedman, and A. Valdes-Garcia, “A 28-GHz 32-element TRX phased-array IC with concurrent dual-polarized operation and orthogonal phase and gain control for 5G communications,” *IEEE Journal of Solid-State Circuits*, vol. 52, no. 12, pp. 3373–3391, 2017.
- [35] M. Kantanen, J. Holmberg, M. Varonen, and A. Rantala, “Digitally controlled vector modulator SiGe MMIC for millimeter-wave phased array applications,” in *2018 11th German Microwave Conference (GeMiC)*, March 2018, pp. 51–54.
- [36] X. Luo, J. Ouyang, Z.-H. Chen, Y. Yan, L. Han, Z. Wu, T. Yu, and K. Zheng, “A scalable Ka-band 1024-element transmit dual-circularly-polarized planar phased array for satcom application,” *IEEE Access*, vol. 8, pp. 156 084–156 095, 2020.
- [37] H. Kähkönen, J. Ala-Laurinaho, and V. Viikari, “Surface-mounted Ka-band Vivaldi antenna array,” *IEEE Open Journal of Antennas and Propagation*, vol. 2, pp. 126–137, 2021.
- [38] M. K. Leino, R. Montoya Moreno, J. Ala-Laurinaho, R. Valkonen, and V. Viikari, “Waveguide-based phased array with integrated element-specific electronics for 28 GHz,” *IEEE Access*, vol. 7, pp. 90 045–90 054, 2019.
- [39] D.-F. Guan, C. Ding, Z.-P. Qian, Y.-S. Zhang, W.-Q. Cao, and E. Dutkiewicz, “An SIW-based large-scale corporate-feed array antenna,” *IEEE Transactions on Antennas and Propagation*, vol. 63, no. 7, pp. 2969–2976, 2015.
- [40] Y. Zhang, S. Christie, V. Fusco, R. Cahill, G. Goussetis, and D. Linton, “Reconfigurable beam forming using phase-aligned Rotman lens,” *IET Microwaves, Antennas Propagation*, vol. 6, no. 3, pp. 326–330, 2012.
- [41] N. T. Nguyen, R. Sauleau, M. Ettorre, and L. Le Coq, “Focal array fed dielectric lenses: An attractive solution for beam reconfiguration at millimeter waves,” *IEEE Transactions on Antennas and Propagation*, vol. 59, no. 6, pp. 2152–2159, 2011.

- [42] A. Mozharovskiy, A. Artemenko, A. Sevastyanov, V. Ssorin, and R. Maslennikov, "Beam-steerable integrated lens antenna with waveguide feeding system for 71-76/81-86 GHz point-to-point applications," in *2016 10th European Conference on Antennas and Propagation (EuCAP)*, April 2016, pp. 1–5.
- [43] A. Lamminen, J. Säily, M. Kaunisto, M. Pokorný, J. Aurinsalo, and Z. Raida, "Gain enhanced millimetre-wave beam-switching Rotman lens antenna designs on LCP," in *2017 11th European Conference on Antennas and Propagation (EuCAP)*, March 2017, pp. 2781–2785.
- [44] C. W. Byeon and C. S. Park, "Design and analysis of the millimeter-wave SPDT switch for TDD applications," *IEEE Transactions on Microwave Theory and Techniques*, vol. 61, no. 8, pp. 2858–2864, 2013.
- [45] J. Ala-Laurinaho, J. Aurinsalo, A. Karttunen, M. Kaunisto, A. Lamminen, J. Nurmiharju, A. V. Räisänen, J. Säily, and P. Wainio, "2-D beam-steerable integrated lens antenna system for 5G E-band access and backhaul," *IEEE Transactions on Microwave Theory and Techniques*, vol. 64, no. 7, pp. 2244–2255, July 2016.
- [46] M. Heino, C. Icheln, J. Haarla, and K. Haneda, "PCB-Based design of a beam-steerable array with high-gain antennas and a Rotman lens at 28 GHz," *IEEE Antennas and Wireless Propagation Letters*, pp. 1–1, 2020.
- [47] J. Butler, "Digital, matrix and intermediate-frequency scanning," in *1965 Antennas and Propagation Society International Symposium*, vol. 3, 1965, pp. 66–70.
- [48] N. J. G. Fonseca, "Printed S-band  $4 \times 4$  Nolen matrix for multiple beam antenna applications," *IEEE Transactions on Antennas and Propagation*, vol. 57, no. 6, pp. 1673–1678, 2009.
- [49] S. Mosca, F. Bilotti, A. Toscano, and L. Vegni, "A novel design method for blass matrix beam-forming networks," *IEEE Transactions on Antennas and Propagation*, vol. 50, no. 2, pp. 225–232, 2002.
- [50] W. Rotman and R. Turner, "Wide-angle microwave lens for line source applications," *IEEE Transactions on Antennas and Propagation*, vol. 11, no. 6, pp. 623–632, 1963.
- [51] Y. J. Cheng, W. Hong, K. Wu, Z. Q. Kuai, C. Yu, J. X. Chen, J. Y. Zhou, and H. J. Tang, "Substrate integrated waveguide (SIW) Rotman lens and its Ka-band multibeam array antenna applications," *IEEE Transactions on Antennas and Propagation*, vol. 56, no. 8, pp. 2504–2513, 2008.
- [52] Y. F. Wu, Y. J. Cheng, and Z. X. Huang, "Ka-band near-field-focused 2-D steering antenna array with a focused Rotman lens," *IEEE Transactions on Antennas and Propagation*, vol. 66, no. 10, pp. 5204–5213, 2018.
- [53] D. F. Filipovic, G. P. Gauthier, S. Raman, and G. M. Rebeiz, "Off-axis properties of silicon and quartz dielectric lens antennas," *IEEE Transactions on Antennas and Propagation*, vol. 45, no. 5, pp. 760–766, May 1997.
- [54] B. Fuchs, O. Lafond, S. Rondineau, M. Himdi, and L. L. Coq, "Off-axis performances of half Maxwell fish-eye lens antennas at 77 GHz," *IEEE Transactions on Antennas and Propagation*, vol. 55, no. 2, pp. 479–482, 2007.
- [55] D. T. Emerson, "The work of Jagadis Chandra Bose: 100 years of millimeter-wave research," *IEEE Transactions on Microwave Theory and Techniques*, vol. 45, no. 12, pp. 2267–2273, 1997.
- [56] O. J. Lodge and J. L. Howard, "On electric radiation and its concentration by lenses," *Proceedings of the Physical Society of London*, vol. 10, no. 1, pp. 143–163, jun 1888. [Online]. Available: <https://doi.org/10.1088/1478-7814/10/1/324>

- [57] A. Boriskin and R. Sauleau, *Aperture antennas for millimeter and sub-millimeter wave applications*. Springer, 2017.
- [58] G. M. Rebeiz, "Millimeter-wave and terahertz integrated circuit antennas," *Proceedings of the IEEE*, vol. 80, no. 11, pp. 1748–1770, Nov 1992.
- [59] T. Cheston and E. J. Luoma, "Constant-k lenses," in *APL Technical Digest*, Mar. 1963, pp. 8–11.
- [60] A. Karttunen, J. Ala-Laurinaho, R. Sauleau, and A. V. Räisänen, "Optimal eccentricity of a low permittivity integrated lens for a high-gain beam-steering antenna," in *Proceedings of the 5th European Conference on Antennas and Propagation (EUCAP)*, April 2011, pp. 3522–3526.
- [61] A. Bisognin, D. Titz, F. Ferrero, G. Jacquemod, R. Pilard, F. Giancesello, D. Gloria, D. Lugara, E. B. Lima, J. R. Costa, C. A. Fernandes, and C. Luxey, "Noncollimating mmw polyethylene lens mitigating dual-source offset from a Tx/Rx WiGig module," *IEEE Transactions on Antennas and Propagation*, vol. 63, no. 12, pp. 5908–5913, 2015.
- [62] C. A. Fernandes, E. B. Lima, and J. R. Costa, "Broadband integrated lens for illuminating reflector antenna with constant aperture efficiency," *IEEE Transactions on Antennas and Propagation*, vol. 58, no. 12, pp. 3805–3813, 2010.
- [63] J. R. Costa, C. A. Fernandes, G. Godi, R. Sauleau, L. Le Coq, and H. Legay, "Compact Ka-band lens antennas for LEO satellites," *IEEE Transactions on Antennas and Propagation*, vol. 56, no. 5, pp. 1251–1258, 2008.
- [64] N. T. Nguyen, R. Sauleau, C. M. Perez, and M. Ettorre, "Finite-difference time-domain simulations of the effects of air gaps in double-shell extended hemispherical lenses," *IET microwaves, antennas & propagation*, vol. 4, no. 1, pp. 35–42, 2010.
- [65] A. Bisognin, D. Titz, F. Ferrero, R. Pilard, C. A. Fernandes, J. R. Costa, C. Corre, P. Calascibetta, J.-M. Rivi re, A. Poulain, C. Badard, F. Giancesello, C. Luxey, P. Busson, D. Gloria, and D. Belot, "3D printed plastic 60 GHz lens: Enabling innovative millimeter wave antenna solution and system," in *2014 IEEE MTT-S International Microwave Symposium (IMS2014)*, 2014, pp. 1–4.
- [66] A. Bisognin, D. Titz, C. Luxey, G. Jacquemod, F. Ferrero, D. Lugara, A. Bisognin, R. Pilard, F. Giancesello, D. Gloria, J. R. Costa, C. Laporte, H. Ezzeddine, E. B. Lima, and C. A. Fernandes, "A 120 GHz 3D-printed plastic elliptical lens antenna with an IPD patch antenna source," in *2014 IEEE International Conference on Ultra-WideBand (ICUWB)*, 2014, pp. 171–174.
- [67] D. F. Filipovic, S. S. Gearhart, and G. M. Rebeiz, "Double-slot antennas on extended hemispherical and elliptical silicon dielectric lenses," *IEEE Transactions on Microwave Theory and Techniques*, vol. 41, no. 10, pp. 1738–1749, Oct 1993.
- [68] A. Karttunen, J. Ala-Laurinaho, R. Sauleau, and A. V. R is nen, "Reduction of internal reflections in integrated lens antennas for beam-steering," *Progress in Electromagnetics Research*, vol. 134, pp. 63–78, 2013.
- [69] A. V. Boriskin, R. Sauleau, and A. I. Nosich, "Performance of hemielliptic dielectric lens antennas with optimal edge illumination," *IEEE Transactions on Antennas and Propagation*, vol. 57, no. 7, pp. 2193–2198, 2009.
- [70] P. J. I. D. M. M. J. M. Van Der Vorst and M. H. H. Herben, "Influence of internal reflections on the far-field pattern of integrated lens antennas," in *Proceedings of the international symposium on antennas and propagation*, vol. 4, Japan, 1996, pp. 1225–1228.

- [71] X. Wu, G. Eleftheriades, and T. van Deventer-Perkins, "Design and characterization of single- and multiple-beam mm-wave circularly polarized substrate lens antennas for wireless communications," *IEEE Transactions on Microwave Theory and Techniques*, vol. 49, no. 3, pp. 431–441, 2001.
- [72] N. T. Nguyen, R. Sauleau, and C. J. Martinez Perez, "Very broadband extended hemispherical lenses: Role of matching layers for bandwidth enlargement," *IEEE Transactions on Antennas and Propagation*, vol. 57, no. 7, pp. 1907–1913, 2009.
- [73] N. T. Nguyen, N. Delhote, M. Ettorre, D. Baillargeat, L. Le Coq, and R. Sauleau, "Design and characterization of 60-GHz integrated lens antennas fabricated through ceramic stereolithography," *IEEE Transactions on Antennas and Propagation*, vol. 58, no. 8, pp. 2757–2762, 2010.
- [74] J. Ala-Laurinaho, A. Karttunen, J. Säily, A. Lamminen, R. Sauleau, and A. V. Räisänen, "Mm-wave lens antenna with an integrated LTCC feed array for beam steering," in *Proceedings of the Fourth European Conference on Antennas and Propagation*, 2010, pp. 1–5.
- [75] A. Artemenko, A. Maltsev, A. Mozharovskiy, A. Sevastyanov, V. Ssorin, and R. Maslennikov, "Millimeter-wave electronically steerable integrated lens antennas for WLAN/WPAN applications," *IEEE Transactions on Antennas and Propagation*, vol. 61, no. 4, pp. 1665–1671, 2013.
- [76] M. Imbert, J. Romeu, M. Baquero-Escudero, M. Martinez-Ingles, J. Molina-Garcia-Pardo, and L. Jofre, "Assessment of LTCC-based dielectric flat lens antennas and switched-beam arrays for future 5G millimeter-wave communication systems," *IEEE Transactions on Antennas and Propagation*, vol. 65, no. 12, pp. 6453–6473, Dec 2017.
- [77] J. R. Costa, M. G. Silveirinha, and C. A. Fernandes, "Evaluation of a double-shell integrated scanning lens antenna," *IEEE Antennas and Wireless Propagation Letters*, vol. 7, pp. 781–784, 2008.
- [78] B. Fuchs, O. Lafond, S. Palud, L. Le Coq, M. Himdi, M. C. Buck, and S. Rondineau, "Comparative design and analysis of Luneburg and half Maxwell fish-eye lens antennas," *IEEE Transactions on Antennas and Propagation*, vol. 56, no. 9, pp. 3058–3062, Sep. 2008.
- [79] Z. Qu, S. Qu, Z. Zhang, S. Yang, and C. H. Chan, "Wide-angle scanning lens fed by small-scale antenna array for 5G in millimeter-wave band," *IEEE Transactions on Antennas and Propagation*, vol. 68, no. 5, pp. 3635–3643, 2020.
- [80] N. T. Nguyen, A. Rolland, A. V. Boriskin, G. Valerio, L. L. Coq, and R. Sauleau, "Size and weight reduction of integrated lens antennas using a cylindrical air cavity," *IEEE Transactions on Antennas and Propagation*, vol. 60, no. 12, pp. 5993–5998, Dec 2012.
- [81] K. X. Wang and H. Wong, "Design of a wideband circularly polarized millimeter-wave antenna with an extended hemispherical lens," *IEEE Transactions on Antennas and Propagation*, vol. 66, no. 8, pp. 4303–4308, 2018.
- [82] A. Mozharovskiy, A. Artemenko, O. Soykin, and R. Maslennikov, "Lens array antenna for 71–76/81–86 GHz point-to-point applications," in *2016 European Radar Conference (EuRAD)*, 2016, pp. 413–416.
- [83] M. R. Dehghani Kodnoeih, Y. Letestu, R. Sauleau, E. Motta Cruz, and A. Doll, "Compact folded fresnel zone plate lens antenna for mm-wave communications," *IEEE Antennas and Wireless Propagation Letters*, vol. 17, no. 5, pp. 873–876, May 2018.

- [84] A. V. Boriskin and R. Sauleau, "Numerical investigation into the design of shaped dielectric lens antennas with improved angular characteristics," *Progress In Electromagnetics Research*, vol. 30, pp. 279–292, 2011.
- [85] N. T. Nguyen, M. Casaletti, T. V. La, and R. Sauleau, "Synthesized elliptical lens with optimized extension for focal array fed lens antennas," in *2012 6th European Conference on Antennas and Propagation (EUCAP)*, 2012, pp. 3295–3298.
- [86] N. T. Nguyen, A. V. Boriskin, L. L. Coq, and R. Sauleau, "Improvement of the scanning performance of the extended hemispherical integrated lens antenna using a double lens focusing system," *IEEE Transactions on Antennas and Propagation*, vol. 64, no. 8, pp. 3698–3702, Aug 2016.
- [87] E. Gandini, A. Tamminen, A. Luukanen, and N. Llombart, "Wide field of view inversely magnified dual-lens for near-field submillimeter wavelength imagers," *IEEE Transactions on Antennas and Propagation*, vol. 66, no. 2, pp. 541–549, 2018.
- [88] E. Gandini, F. Silvestri, A. Benini, G. Gerini, E. Martini, S. Maci, M. C. Viganò, G. Toso, and S. Monni, "A dielectric dome antenna with reduced profile and wide scanning capability," *IEEE Transactions on Antennas and Propagation*, vol. 69, no. 2, pp. 747–759, 2021.
- [89] M. J. M. van der Vorst, P. J. I. de Maagt, and M. H. A. J. Herben, "Scan-optimized integrated lens antennas," in *1997 27th European Microwave Conference*, vol. 1, Jerusalem, Isarel, Sept 1997, pp. 605–610.
- [90] A. Karttunen, J. Ala-Laurinaho, R. Sauleau, and A. V. Räisänen, "Extended hemispherical integrated lens antenna with feeds on a spherical surface," in *2013 7th European Conference on Antennas and Propagation (EuCAP)*, April 2013, pp. 2539–2543.
- [91] B. Fuchs, L. Le Coq, O. Lafond, S. Rondineau, and M. Himdi, "Design optimization of multishell Luneburg lenses," *IEEE Transactions on Antennas and Propagation*, vol. 55, no. 2, pp. 283–289, 2007.
- [92] M. K. Saleem, H. Vettikaladi, M. A. S. Alkanhal, and M. Himdi, "Lens antenna for wide angle beam scanning at 79 GHz for automotive short range radar applications," *IEEE Transactions on Antennas and Propagation*, vol. 65, no. 4, pp. 2041–2046, April 2017.
- [93] J. Bor, O. Lafond, B. Fuchs, H. Merlet, P. Le Bars, and M. Himdi, "Light and cheap flat foam-based Luneburg lens antenna," in *The 8th European Conference on Antennas and Propagation (EuCAP 2014)*, 2014, pp. 3200–3204.
- [94] O. Quevedo-Teruel, J. Miao, M. Mattsson, A. Algaba-Brazalez, M. Johansson, and L. Manholm, "Glide-symmetric fully metallic Luneburg lens for 5G communications at Ka-band," *IEEE Antennas and Wireless Propagation Letters*, vol. 17, no. 9, pp. 1588–1592, 2018.
- [95] N. J. G. Fonseca, Q. Liao, and O. Quevedo-Teruel, "Equivalent planar lens ray-tracing model to design modulated geodesic lenses using non-euclidean transformation optics," *IEEE Transactions on Antennas and Propagation*, vol. 68, no. 5, pp. 3410–3422, 2020.
- [96] G. C. Trichopoulos, G. Mumcu, K. Sertel, H. L. Mosbacker, and P. Smith, "A novel approach for improving off-axis pixel performance of terahertz focal plane arrays," *IEEE Transactions on Microwave Theory and Techniques*, vol. 58, no. 7, pp. 2014–2021, 2010.
- [97] A. Artemenko, A. Maltsev, R. Maslennikov, A. Sevastyanov, and V. Ssorin, "Design of silicon integrated lens antenna for 60 GHz indoor wireless communications," in *2010 Conference Proceedings ICECom, 20th International Conference on Applied Electromagnetics and Communications*, 2010, pp. 1–4.

- [98] A. Lamminen, J. Säily, J. Ala-Laurinaho, J. de Cos, and V. Ermolov, "Patch antenna and antenna array on multilayer high-frequency pcb for D-band," *IEEE Open Journal of Antennas and Propagation*, vol. 1, pp. 396–403, 2020.
- [99] J. Edstam, "Microwave backhaul gets a boost with multiband," *Ericsson Technology Review*, pp. 1–11, 2016.
- [100] S. Hur, T. Kim, D. J. Love, J. V. Krogmeier, T. A. Thomas, and A. Ghosh, "Millimeter wave beamforming for wireless backhaul and access in small cell networks," *IEEE Transactions on Communications*, vol. 61, no. 10, pp. 4391–4403, 2013.
- [101] A. Bisognin, N. Nachabe, C. Luxey, F. Ganesello, D. Gloria, J. R. Costa, C. A. Fernandes, Y. Alvarez, A. Arboleya-Arboleya, J. Laviada, F. Las-Heras, N. Dolatsha, B. Grave, M. Sawaby, and A. Arbabian, "Ball grid array module with integrated shaped lens for 5G backhaul/fronthaul communications in F-Band," *IEEE Transactions on Antennas and Propagation*, vol. 65, no. 12, pp. 6380–6394, 2017.
- [102] L. Lu, G. Y. Li, A. L. Swindlehurst, A. Ashikhmin, and R. Zhang, "An overview of massive MIMO: Benefits and challenges," *IEEE Journal of Selected Topics in Signal Processing*, vol. 8, no. 5, pp. 742–758, 2014.
- [103] E. G. Larsson, O. Edfors, F. Tufvesson, and T. L. Marzetta, "Massive MIMO for next generation wireless systems," *IEEE Communications Magazine*, vol. 52, no. 2, pp. 186–195, 2014.
- [104] T. Kwon, Y. Lim, B. Min, and C. Chae, "RF lens-embedded massive MIMO systems: Fabrication issues and codebook design," *IEEE Transactions on Microwave Theory and Techniques*, vol. 64, no. 7, pp. 2256–2271, 2016.
- [105] J. Brady, N. Behdad, and A. M. Sayeed, "Beamspace MIMO for millimeter-wave communications: System architecture, modeling, analysis, and measurements," *IEEE Transactions on Antennas and Propagation*, vol. 61, no. 7, pp. 3814–3827, 2013.
- [106] ETSI, "Fixed radio system; characteristics and requirement for point-to-point equipment and antennas," European Telecommunications Standards Institute, Tech. Rep., 2008.
- [107] J. W. Lamb, "Miscellaneous data on materials for millimetre and submillimetre optics," *International Journal of Infrared and Millimeter Waves*, vol. 17, no. 12, pp. 1997–2034, 1996.
- [108] B. Schoenlinner, X. Wu, J. Ebling, G. Eleftheriades, and G. Rebeiz, "Wide-scan spherical-lens antennas for automotive radars," *IEEE Transactions on Microwave Theory and Techniques*, vol. 50, no. 9, pp. 2166–2175, 2002.
- [109] W. E. Kock, "Metal-lens antennas," *Proceedings of the IRE*, vol. 34, no. 11, pp. 828–836, Nov 1946.
- [110] J. E. Lawrance, C. G. Christodoulou, and M. R. Taha, "A high-power microwave zoom antenna with metal-plate lenses," *IEEE Transactions on Antennas and Propagation*, vol. 63, no. 8, pp. 3380–3389, 2015.
- [111] V. Pacheco-Peña, B. Orazbayev, U. Beaskoetxea, M. Beruete, and M. Navarro-Cía, "Zoned near-zero refractive index fishnet lens antenna: Steering millimeter waves," *Journal of Applied Physics*, vol. 115, no. 12, p. 124902, 2014.
- [112] H. Onoue, N. Kamiya, R. Suga, and O. Hashimoto, "Broadband metal-plate lens with short focal length," in *2013 European Radar Conference*, Oct 2013, pp. 363–366.
- [113] R. J. Stegen, "Longitudinal shunt slot characteristics," *Hughes Technical Memorandum No. 261*, vol. 261, no. 1, pp. 1–21, 1951.

# Errata

## Publication IV

The x-axis label of Figure 8 should be "Frequency (GHz)" instead of  $\theta^\circ$ .





The dissertation focuses on the development of high gain antennas based on beam-switching topology at millimeter-wave frequencies. Primarily, the research aims to make an integrated lens antenna low-profile, minimize scan loss, and improve efficiency. Secondly, the feeding network of the beam-switching antenna is studied to understand the impact of the feed array coupling, achieve beam-reconfigurability and mitigate insertion loss in the switching network.



ISBN 978-952-64-0539-1 (printed)

ISBN 978-952-64-0540-7 (pdf)

ISSN 1799-4934 (printed)

ISSN 1799-4942 (pdf)

**Aalto University**  
**School of Electrical Engineering**  
**Department of Electronics and Nanoengineering**  
[www.aalto.fi](http://www.aalto.fi)

**BUSINESS +  
ECONOMY**

**ART +  
DESIGN +  
ARCHITECTURE**

**SCIENCE +  
TECHNOLOGY**

**CROSSOVER**

**DOCTORAL  
DISSERTATIONS**